



**US Army Corps
of Engineers**
Waterways Experiment
Station

Technical Report HL-93-12
August 1993

AD-A270 182



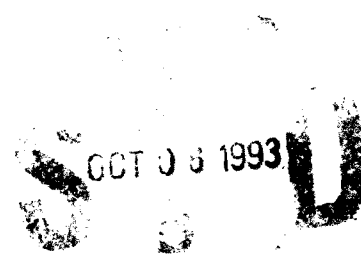
2

In-House Laboratory Independent Research Program

A Finite Element Scheme for Shock Capturing

by *R. C. Berger, Jr.*
Hydraulics Laboratory

Approved For Public Release; Distribution Is Unlimited



93-23268



6308

Prepared for Assistant Secretary of the Army (R&D)

93 10 5 0 19

The contents of this report are not to be used for advertising, publication, or promotional purposes. Citation of trade names does not constitute an official endorsement or approval of the use of such commercial products.



PRINTED ON RECYCLED PAPER

**In-House Laboratory Independent
Research Program**

**Technical Report HL-93-12
August 1993**

A Finite Element Scheme for Shock Capturing

by **R. C. Berger, Jr.**

Hydraulics Laboratory

**U.S. Army Corps of Engineers
Waterways Experiment Station
3909 Halls Ferry Road
Vicksburg, MS 39180-6199**

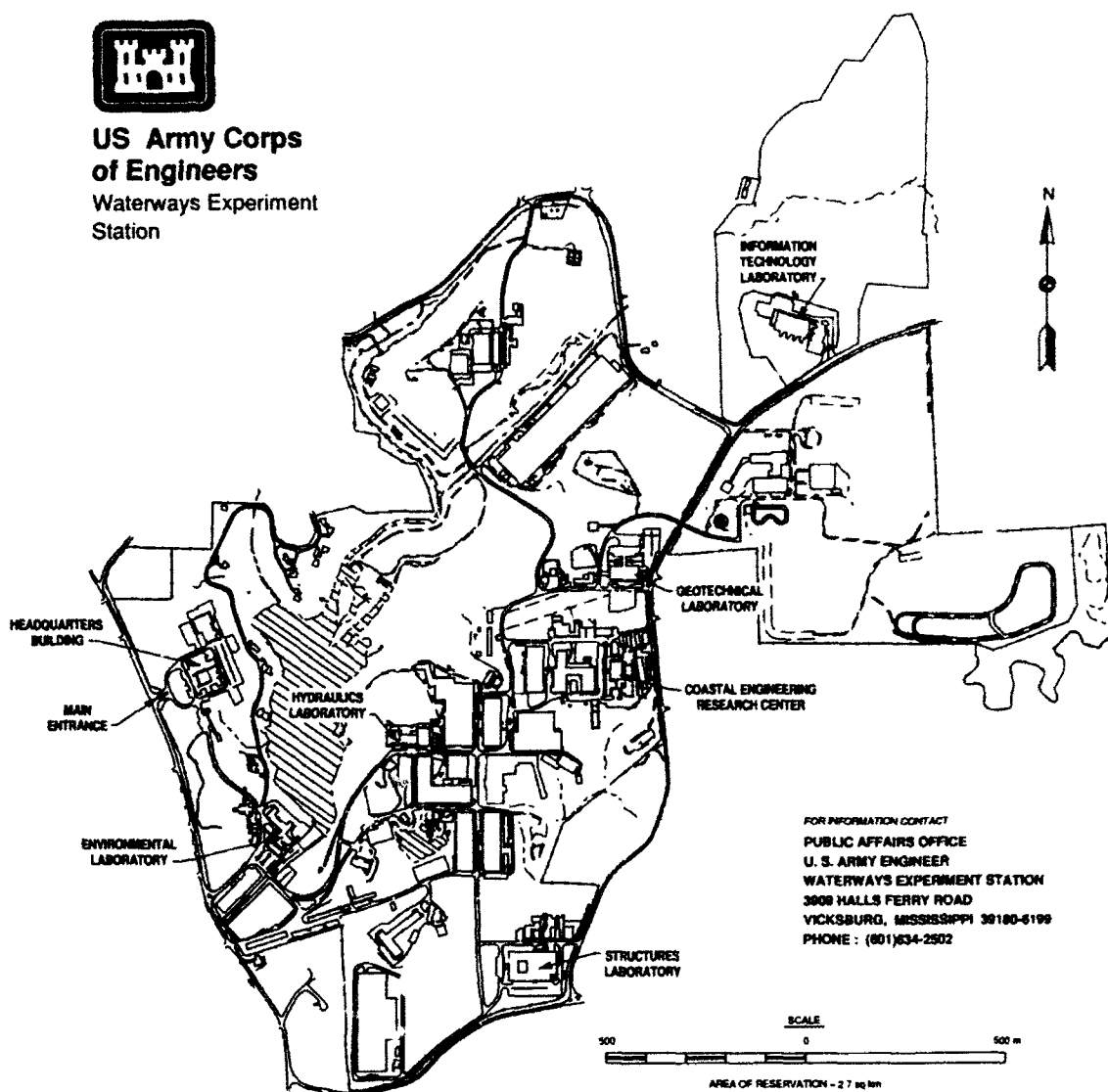
Final report

Approved for public release; distribution is unlimited

**Prepared for Assistant Secretary of the Army (R&D)
Washington, DC 20315**



**US Army Corps
of Engineers**
Waterways Experiment
Station



Waterways Experiment Station Cataloging-In-Publication Data

Berger, Rutherford C.

A finite element scheme for shock capturing / by R.C. Berger, Jr., ; prepared for Assistant Secretary of the Army (R&D).

61 p. : ill. ; 28 cm. — (Technical report ; HL-93-12)

Includes bibliographical references.

1. Hydraulic jump — Mathematical models. 2. Hydrodynamics. 3. Shock (Mechanics) — Mathematical models. 4. Finite element method. I. United States. Assistant Secretary of the Army (Research, Development and Acquisition) II. U.S. Army Engineer Waterways Experiment Station. III. In-house Laboratory Independent Research Program (U.S. Army Engineer Waterways Experiment Station) IV. Title. V. Series: Technical report (U.S. Army Engineer Waterways Experiment Station) ; HL-93-12.

TA7 W34 no HL-93-12

Contents

Preface	iv
1—Introduction	1
Background	1
Basic Equations	2
Shock equations	4
Shock relations in 2-D	9
2—Numerical Approach	13
Advective Dominated Flow	13
The Problem	13
Petrov-Galerkin formulation	14
Shock Capturing	20
3—Testing	23
Case 1: Analytic Shock Speed	24
Case 2: Dam Break	28
Case 3: 2-D Lateral Transition	40
Discussion	43
4—Conclusions	54
References	55
SF 298	

Accession For	
NTIS OMA&I	<input checked="" type="checkbox"/>
DTIC TAB	<input type="checkbox"/>
Unannounced	<input type="checkbox"/>
Justification	
By	
Dist. H. 1000	
Ann. 1000 1000	
Dist	Special
A-1	

DTIC QUALITY INSPECTED 2

Preface

This report is the product of research conducted from January 1992 through April 1993 in the Estuaries Division (ED), Hydraulics Laboratory (HL), U.S. Army Engineer Waterways Experiment Station (WES), under the In-House Laboratory Independent Research (ILIR) Program. The funding was providing by ILIR work unit "Finite Element Scheme for Shock Capturing."

Dr. R. C. Berger, Jr., ED, performed the work and prepared this report under the general supervision of Messrs. F. A. Herrmann, Jr., Director, HL; R. A. Sager, Assistant Director, HL; and W. H. McAnally, Chief, ED.

Mr. Richard Stockstill of the Hydraulic Structures Division, HL, performed the test on supercritical contraction.

At the time of publication of this report, Director of WES was Dr. Robert W. Whalin. Commander was COL Bruce K. Howard, EN.

1 Introduction

Background

Shocks in fluids result from fluid flow that is more rapid than the speed of a compression wave. Thus there is no means for the flow to adjust gradually. Pressure, velocity, and temperatures change abruptly, causing severe fatigue and component destruction in military aircraft and engine turbines. This problem is not limited to supersonic aircraft; many parts of subsonic craft are supersonic. For example, the rotors of helicopters have supersonic regions as do the blades of the turbine engines used on many crafts. The shock is formed as the flow passes from supersonic to subsonic or, in the case of an oblique shock, as the result of a geometric transition in supersonic flow. Wind tunnels are limited in the Mach numbers they can achieve and testing is expensive; thus design relies upon numerical modeling. In hydraulics the equivalent shocks are referred to as hydraulic jumps, surges, and bores. Here, for example, it is important to determine the ultimate height of water resulting from a dam break or the insertion of a bridge in a fast-flowing river.

The compressible Euler equations describe these flow fields and are solved numerically in discrete models. These partial differential equations implicitly assume a certain degree of smoothness in the solution. Models, therefore, have great difficulty handling shocks. One method to avoid solving numerically across the shock is to track the shock and impose an internal boundary there. This method is called "shock-tracking." On the other hand the sharp resolution of the shock can be forfeited and allow for $O(1)$ error at the transition. This is referred to as "shock-capturing," as originated by von Neumann and Richtmyer (1950), and is now the most common technique used in engineering practice.

Great care must be undertaken to make sure the errors are local to the shock. Otherwise the shock location and speed will be incorrect. It is important that the discrete numerical operations preserve the Rankine-Hugoniot condition (Anderson, Tannehill, and Pletcher 1984) resulting from integration by parts. While this should result in reasonable shock speed and location, discrete models commonly suffer from numerical oscillations near the shock.

There are many proposed methods used to reduce these oscillations. The

basic theme is to cleverly apply artificial diffusion as a result of flow parameters. Many of these methods do not preserve the original equations within the shock due to this added diffusion. Hughes and Brooks (1982) have approached this problem within the finite elements method by the development of a single test function that reflects the speed of fluid transport (the SUPG scheme, Streamline Upwind Petrov-Galerkin) to be applied to the entire partial differential equation set. In this manner the model is consistent even at discrete scales. Its application, thus far, has been only to the very simple case of Burgers' equations.

In this report a two-dimensional (2-D) finite element model for the shallow-water equations is produced using an extension of the SUPG concept, but relying upon the characteristics of the advection matrix (transport as well as the free-surface wave speeds) to develop the test function to be applied to the coupled set of equations. The shallow-water equations are a direct analogy to the Euler equations with the depth substituted for density and dropping the energy equation. This equation set is ideal for testing numerical schemes for the Euler equations. The model developed can reproduce supercritical and subcritical flow and is shown to reproduce very difficult conditions of supercritical channel transitions and preserve the Rankine-Hugoniot conditions.

For simple geometries, analytic and flume results are compared with approaches for shock-capturing and shock detection. A trigger mechanism that turns on the capture schemes in the vicinity of shocks and the characteristic upstream weighted test function are tested.

The results of this research are an algorithm and program to represent hydraulic jumps and oblique jumps in 2-D for shallow flow. The code, HIVEL2D, is a general-purpose tool that is applicable to many problems faced in high-velocity hydraulic channels, notably, in the calculation of the ultimate water surface height around bridges, channel bends, and confluences subjected to supercritical flow or due to surges caused by sudden releases or dam failure. The algorithm itself is applicable outside the field of hydraulics as well to complex aerodynamic flow fields containing shocks.

Basic Equations

The basic equations that are addressed are the 2-D shallow-water equations given as:

$$\frac{\partial Q}{\partial t} + \frac{\partial F_x}{\partial x} + \frac{\partial F_y}{\partial y} + H = 0 \quad (1)$$

where

$$Q = \begin{Bmatrix} h \\ p \\ q \end{Bmatrix}$$

$$F_x = \begin{Bmatrix} p \\ \frac{p^2}{h} + \frac{1}{2} gh^2 - \frac{h\sigma_{11}}{\rho} \\ \frac{pq}{h} - \frac{h\sigma_{21}}{\rho} \end{Bmatrix}$$

$$F_y = \begin{Bmatrix} q \\ \frac{pq}{h} - \frac{h\sigma_{12}}{\rho} \\ \frac{q^2}{h} + \frac{1}{2} gh^2 - \frac{h\sigma_{22}}{\rho} \end{Bmatrix}$$

$$H = \begin{Bmatrix} 0 \\ ghe_1 + gp \frac{n^2(p^2 + q^2)^{1/2}}{c^2 h^{7/3}} \\ ghe_2 + gq \frac{n^2(p^2 + q^2)^{1/2}}{c^2 h^{7/3}} \end{Bmatrix}$$

where

t = time

x, y = Horizontal Cartesian coordinates

h = depth

p = x-discharge per unit width, uh

q = y-discharge per unit width, vh

g = acceleration due to gravity

$$\sigma_{11} = 2\rho\nu \frac{\partial u}{\partial x}$$

$$\sigma_{12} = \sigma_{21} = \rho\nu \left(\frac{\partial u}{\partial y} + \frac{\partial v}{\partial x} \right)$$

$$\sigma_{22} = 2\rho\nu \frac{\partial v}{\partial y}$$

ρ = fluid density

ν = kinematic viscosity (turbulent and molecular)

u, v = velocity in x, y directions

$$e_1 = \frac{\partial z}{\partial x}$$

z = bed elevation

n = Manning's coefficient

c = 1.0 metric, 1.486 non-SI

$$e_2 = \frac{\partial z}{\partial y}$$

These equations neglect the Coriolis effect and assume the pressure distribution is hydrostatic, and the bed slope is assumed to be geometrically mild though it may be hydraulically steep. These equations apply throughout the domain in which the solution is sufficiently smooth. Now consider the case for which the solution is not smooth.

Shock equations

In this section we first derive the jump conditions in one dimension (1-D) with no dissipative terms, i.e., friction or viscosity. We show that as a result of the discontinuity of the jump, the shallow-water equations should conserve mass and momentum balance but will lose energy. Furthermore, if there is no discontinuity, energy too will be conserved. Later the jump relations are extended to 2-D.

This derivation relies upon the work of Stoker (1957) and Keulegan (1950) following a fluid element through a moving jump. Figure 1 defines these features.

If our coordinate system is chosen to move with the jump at speed V_w , then we may use the following term definitions.

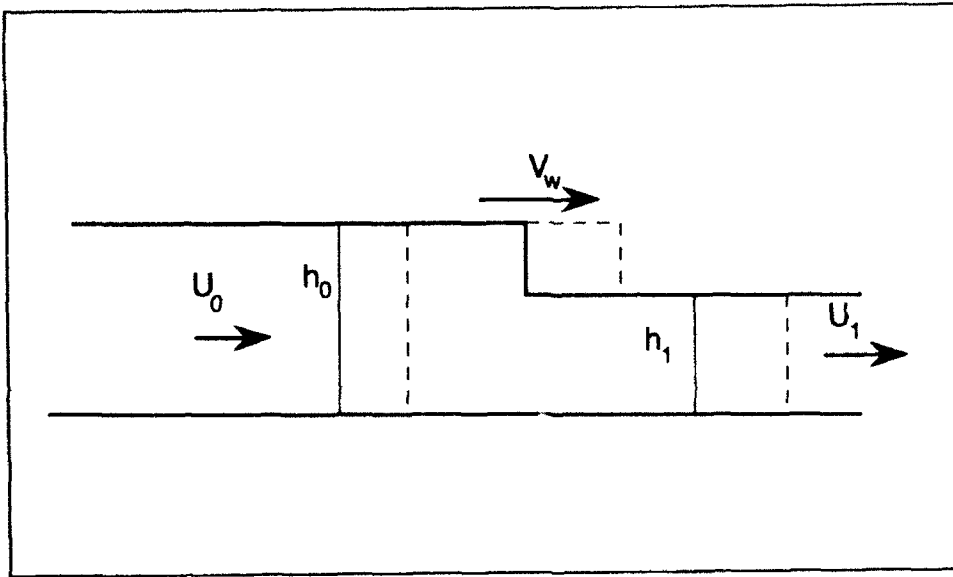


Figure 1. Definition of terms for a moving hydraulic jump

U_0 = velocity at section 0

h_0 = depth at section 0

U_1 = velocity at section 1

h_1 = depth at section 1

$V_0 = U_0 - V_w$, the velocity at section 0 relative to the jump

$V_1 = U_1 - V_w$, relative velocity at section 1

Mass. Now following an infinitesimal fluid element in our moving coordinate system we know that mass is conserved so we have,

$$\frac{d\rho}{dt} = 0 \quad (2)$$

where ρ , the fluid density, is a constant here.

Across the element we have

$$\rho(V_1 h_1 - V_0 h_0) = 0 \quad (3)$$

or

$$V_1 h_1 = V_0 h_0 = q \quad (4)$$

where q is the relative discharge. Equation 3 may be written in a fixed grid as

$$V_w [h] = [Uh] \quad (5)$$

where the symbol $[]$ implies the jump in the quantities across the discontinuity, e.g., $[h] = h_1 - h_0$.

Momentum. In the same manner we show that momentum is conserved by:

$$\frac{d(\rho U)}{dt} = \rho(\bar{P}_0 - \bar{P}_1) \quad (6)$$

$$\rho [(V_1 h_1) U_1 - (V_0 h_0) U_0] = \rho (\bar{P}_0 - \bar{P}_1) \quad (7)$$

where

$$\bar{P}_0 = \frac{1}{2} g h_0^2$$

$$\bar{P}_1 = \frac{1}{2} g h_1^2$$

$$q (U_1 - U_0) = \bar{P}_0 - \bar{P}_1 \quad (8)$$

which in a fixed coordinate system would be:

$$V_w [Uh] = [U^2 h + \bar{P}] \quad (9)$$

Energy. Now consider the case of mechanical energy E as it passes through the discontinuity

$$\begin{aligned} \frac{dE}{dt} = \rho \left[\frac{1}{2} V_1 h_1 U_1^2 - \frac{1}{2} V_0 h_0 U_0^2 + \bar{P}_1 V_1 \right. \\ \left. - \bar{P}_0 V_0 + \bar{P}_1 U_1 - \bar{P}_0 U_0 \right] \end{aligned} \quad (10)$$

If we multiply (8) by V_w add this to (10) using the relationship for q we have:

$$\begin{aligned}\frac{dE}{dt} &= \rho \left[\frac{1}{2} q(V_1^2 - V_0^2) + 2(\bar{P}_1 V_1 - \bar{P}_0 V_0) \right] \\ &= \rho \left[\frac{1}{2} q(V_1 - V_0)(V_1 + V_0) + 2(\bar{P}_1 V_1 - \bar{P}_0 V_0) \right]\end{aligned}\quad (11)$$

Now substituting Equation 8 yields

$$\frac{dE}{dt} = \rho \left[\frac{1}{2} (\bar{P}_0 - \bar{P}_1)(V_1 + V_0) + 2(\bar{P}_1 V_1 - \bar{P}_0 V_0) \right] \quad (12)$$

or, finally

$$\frac{dE}{dt} = \frac{\rho q g}{4} \frac{(h_0 - h_1)^3}{h_0 h_1} \quad (13)$$

so that the shallow-water equations lose energy at the jump, and it is proportional to the depth differential cubed. If the depth is continuous, no energy will be lost.

While mathematically an energy gain, $dE/dt > 0$, through the jump is a possibility, physically it is not. If we restrict ourselves to energy losses through the jump, there are two possible cases.

- a. *Case 1:* $V_0, V_1 < 0$ implies $h_0 > h_1$. The jump progresses downstream through our fluid element (Figure 2).
- b. *Case 2:* $V_0, V_1 > 0$ implies $h_0 < h_1$. The fluid passes downstream through the jump (Figure 3).

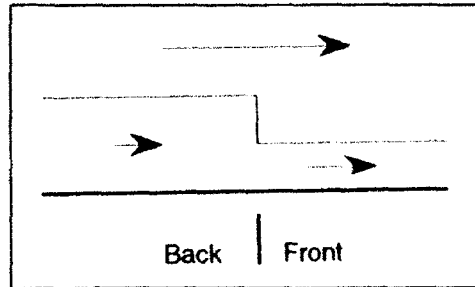


Figure 2. Example of Case 1; jump passes downstream through the fluid element

Here we have arbitrarily chosen the flow to be from left to right, if we had chosen the opposite direction one would simply have horizontal mirror images of Figures 2 and 3. A fluid particle that is about to be swept into or caught by the jump is considered in "front" of the jump. A fluid element that has passed through the jump is now "behind" it. Therefore, we may conclude that the water level is lower in front of the jump than it is behind the jump.

In order to calculate the wave speed, it is convenient to choose $U_1 = 0$.

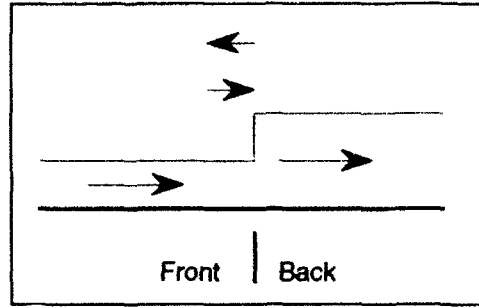


Figure 3. Example of Case 2; the fluid passes downstream through the jump

This is completely arbitrary, and this form also produces an easy test case that will be eventually applied to the numerical model. With $U_1 = 0$, then $V_1 = U_1 - V_w = -V_w$, the momentum equation may be written as:

$$-V_w(U_0 - V_w) = \frac{1}{2}g(h_0 + h_1) \quad (14)$$

and now, taking advantage of our mass conservation relationship, we have:

$$-V_w \frac{h_1}{h_0} = U_0 - V_w \quad (15)$$

We may substitute for U_0 to yield:

$$V_w = - \left[g \frac{h_0}{h_1} \left(\frac{h_0 + h_1}{2} \right) \right]^{1/2} \quad (16)$$

If we consider the speed of the perturbation in front of and behind the shock, we note that both move toward the shock.

To demonstrate this, we calculate the relative speeds V_0 and V_1 . These are the speeds of fluid particles as perceived by an observer moving with the shock. We have already shown that $V_1 = -V_w$ or

$$V_1 = + \left[\frac{1}{2} g \frac{h_0}{h_1} (h_0 + h_1) \right]^{1/2} \quad (17)$$

The relative speed of an upstream moving perturbation W_1 is

$$W_1 = U_1 - \sqrt{gh_1} - V_w = V_1 - \sqrt{gh_1} \quad (18)$$

If this value is negative, then a perturbation behind the jump catches the shock, and from Equation 17 we know $\sqrt{gh_1}$ is greater in magnitude than V_1 , $W_1 < 0$.

In front of the shock the relative particle speed is V_0 .

$$V_0 h_0 = V_1 h_1 \quad (19)$$

$$V_0 = -V_w \frac{h_1}{h_0} \quad (20)$$

$$V_0 = \left[\frac{1}{2} g \frac{h_1}{h_0} (h_0 + h_1) \right]^{1/2} \quad (21)$$

Again we calculate the relative speed of a perturbation, but now in front of the shock:

$$W_0 = U_0 - \sqrt{gh_0} - V_w = V_0 - \sqrt{gh_0} \quad (22)$$

Now if W_0 is positive the shock catches up with the wave perturbation, and since V_0 is clearly greater than $\sqrt{gh_0}$ this is indeed what happens. Therefore any small perturbations are swept toward, and are engulfed in the shock.

Shock relations in 2-D

Previous sections derive the shock relations in 1-D and are important for understanding behavior and to produce test problems. Here we extend these relations to 2-D (Courant and Friedrichs 1948). To do this, consider the region Ω shown in Figure 4. It is divided into subdomains Ω_1 and Ω_2 by the shock shown as boundary Γ_s , which is defined by the coordinate location $X_s(t)$. The right side boundary is Γ_r and the left Γ_l . The normal direction is chosen as shown in Figure 4. Integration over the subdomains is performed separately; and then by letting the width about the shock go to zero, we derive the mass and momentum relationship across the jump in the direction n .

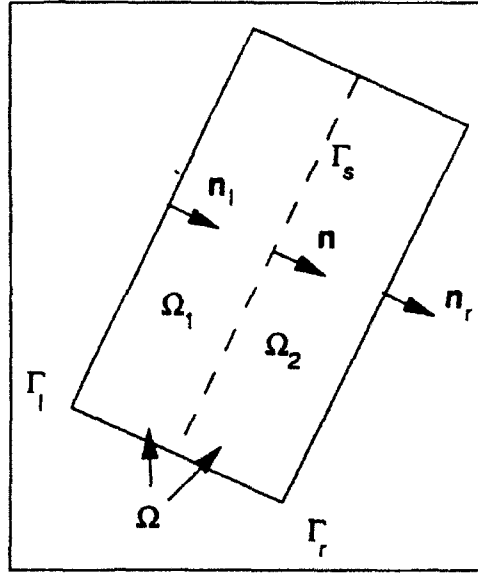


Figure 4. Definition of terms for 2-D shock

Mass conservation. For constant density we have

$$\frac{d}{dt} \int_{\Omega_1} h \, d\Omega + \frac{d}{dt} \int_{\Omega_2} h \, d\Omega = 0 \quad (23)$$

which may be expanded as

$$\begin{aligned} \int_{\Omega_1} \frac{\partial h}{\partial t} d\Omega + \int_{\Omega_2} \frac{\partial h}{\partial t} d\Omega - \int_{\Gamma_l} h_l (V_l \cdot n_l) d\Gamma + \int_{\Gamma_s} h^- [\dot{X}_s(t) \cdot n] d\Gamma \\ - \int_{\Gamma_s} h^+ [\dot{X}_s(t) \cdot n] d\Gamma + \int_{\Gamma_r} h_r (V_r \cdot n_r) d\Gamma = 0 \end{aligned} \quad (24)$$

where,

V_l = the velocity of the left boundary

V_r = the velocity of the right boundary

$\dot{X}_s(t)$ = the velocity of the shock

h^- = the depth in the limit as the shock is approached
from subdomain Ω_1

h^+ = the depth in the limit as the shock is approached
from subdomain Ω_2

Taking the limit as Ω_1 and Ω_2 shrink in width we have

$$\int_{\Gamma_s} \left\{ h^- [V^- - \dot{X}_s(t)] \cdot n - h^+ [V^+ - \dot{X}_s(t)] \cdot n \right\} d\Gamma = 0 \quad (25)$$

where,

V^- = the velocity in the limit as the shock is
approached in subdomain Ω_1

V^+ = the velocity in the limit as the shock is
approached in subdomain Ω_2

For an arbitrary segment Γ_s to preserve the equation, the integrand itself must satisfy the equation, therefore

$$[hV_s] = 0 \quad (26)$$

where

$$V_s^- = [V^- - \dot{X}_s(t)] \cdot n \quad (27)$$

$$V_s^+ = [V^+ - \dot{X}_s(t)] \cdot n \quad (28)$$

which states that the relative mass flux jump across the shock in the direction \mathbf{n} should be zero.

Momentum relation. Again assuming constant density, the balance of momentum and force may be written as (in the direction of the normal to the shock)

$$\begin{aligned} \frac{d}{dt} \int_{\Omega_1} Vh \cdot n \, d\Omega + \frac{d}{dt} \int_{\Omega_2} Vh \cdot n \, d\Omega = & - \int_{\Gamma_r} \frac{1}{2} gh_r^2 n \cdot n_r \, d\Gamma \\ & + \int_{\Gamma_t} \frac{1}{2} gh_t^2 n \cdot n_t \, d\Gamma \end{aligned} \quad (29)$$

$$\begin{aligned} \int_{\Omega_1} \frac{\partial}{\partial t} (Vh \cdot n) \, d\Omega + \int_{\Omega_2} \frac{\partial}{\partial t} (Vh \cdot n) \, d\Omega - \int_{\Gamma_t} (V_t h_t \cdot n_t) (V_t \cdot n) \, d\Gamma \\ + \int_{\Gamma_s} (V^- h^- \cdot n) [\dot{X}_s(t) \cdot n] \, d\Gamma - \int_{\Gamma_s} (V^+ h^+ \cdot n) [\dot{X}_s(t) \cdot n] \, d\Gamma \end{aligned} \quad (30)$$

$$\begin{aligned} + \int_{\Gamma_r} (V_r h_r \cdot n_r) (V_r \cdot n) \, d\Gamma = & - \int_{\Gamma_r} \frac{1}{2} gh_r^2 n \cdot n_r \, d\Gamma \\ & + \int_{\Gamma_t} \frac{1}{2} gh_t^2 n \cdot n_t \, d\Gamma \end{aligned}$$

and taking the limit as Ω_1 and Ω_2 shrink in width results in

$$\begin{aligned}
& \int_{\Gamma_s} \left\{ - (V^- h^- \cdot n) [V^- - \dot{X}_s(t)] \cdot n + (V^+ h^+ \cdot n) [V^+ - \dot{X}_s(t)] \cdot n \right\} d\Gamma \\
& \qquad \qquad \qquad (31) \\
& = - \int_{\Gamma_s} \frac{1}{2} g \left[(h^+)^2 - (h^-)^2 \right] d\Gamma
\end{aligned}$$

which for an arbitrary length Γ_s to preserve the equation, the integrand itself must satisfy the equation, therefore:

$$- (Q^- \cdot n) V_s^- + (Q^+ \cdot n) V_s^- + \frac{1}{2} g \left[(h^+)^2 - (h^-)^2 \right] = 0 \quad (32)$$

where,

$$Q^- = V^- h^-$$

$$Q^+ = V^+ h^+$$

or

$$[(Q \cdot n) V_s + \frac{1}{2} g h^2] = 0 \quad (33)$$

which states that the relative momentum flux in the direction n is balanced by the pressure jump across the shock.

2 Numerical Approach

The selection of a numerical scheme is driven by two related difficulties: numerically modeling highly advective flow and the capturing of shocks. This chapter discusses the problem with advection schemes generally. It then follows the development of the scheme we will use and discusses the implications in shock capturing.

Advection Dominated Flow

The problem

The quality of the numerical solution depends upon the choice of the basis (or interpolation) function and upon the test function. The basis function determines how the variable (or solution) is represented and the test function determines the way in which the differential equation is enforced. Finite elements are a subset of the weighted residual method. Here one looks at the solution of a differential equation in a weighted average sense. In the Galerkin approach the test function is identical to the basis function. This method can have difficulty with advection-dominated flow. The basic problem is that the form of the test function (typically an even or symmetric function) cannot detect the presence of a node-to-node oscillation, since this "spurious solution" has a spatial derivative which is an odd function (antisymmetric). One approach to resolve this problem is to use a mixed interpolation where, for the shallow-water equations, the depth uses a lower order basis than does the velocity (see, e.g., Platzman (1978) or Walters and Carey (1983)). Typically, these are chosen as depth as an elemental constant and velocity as linear, or depth linear and velocity as a quadratic. This approach effectively decouples the depth from this node-to-node oscillation but depends upon some additional artificial viscosity to damp velocity oscillations if the flow is not highly resolved. Another approach is to modify the test function so that it includes odd functions as well as even functions so that these modes can be detected and if weighted properly, eliminated. Any approach in which the test function differs from the basis function is termed a Petrov-Galerkin approach. In our case we choose the Lagrange basis functions to be C^0 ; i.e., the functions are continuous. Let us consider an example to illustrate the problem with the Galerkin approach and an approach to develop a Petrov-Galerkin test function.

Petrov-Galerkin formulation

First we will illustrate the problem that discrete formulations have with advection-dominated flow. In this regard the 1-D linearized inviscid Burgers' equation may be written

$$C_t + U_0 C_x = 0, \text{ over domain } L \quad (34)$$

where the subscripts t and x represent partial derivatives with respect to time and space, respectively, and

U_0 = the advection velocity, which here is a constant

C = some species concentration

In the discrete representation we shall approximate the solution as C° linear Lagrange basis functions,

$$\tilde{C}(x) = \sum_j \phi_j(x) C_j$$

here $\tilde{C}(x)$ is the approximate solution, and the subscript j indicates nodal values and ϕ_j is the Galerkin test function at node j .

Our numerical solution equation, for the steady-state problem ($C_t=0$) may be written as the inner product

$$(\phi_i, U_0 \sum_j \phi_j'(x) C_j) = 0, \text{ for each } i \quad (35)$$

where

$$(f(x), g(x)) = \int_L f(x) g(x) dx$$

and the prime indicates the derivative with respect to x .

On a uniform grid the result of this integration on a typical patch is

$$C_{j+1} - C_{j-1} = 0 \quad (36)$$

(Note that finite difference methods using central differences give an identical result.)

In order to demonstrate that this solution contains a spurious oscillation, let's write these nodal values as

$$C_j = \hat{C} \rho^j \quad (37)$$

where \hat{C} is a constant determined by the boundary condition and ρ is the numerical root.

The roots of Equation 36 are

$$\rho^2 - 1 = 0 \quad (38)$$

or

$$\rho = \pm 1 \quad (39)$$

which makes the general solution

$$C_j = \hat{C} + b [-1]^j \quad (40)$$

where b is some constant.

The analytic solution corresponds to $\rho = 1$. The spurious node-to-node oscillation is the root $\rho = -1$. This root results from a test function which is made up solely of even functions; that is, the test function, the hat function, is symmetric about node i (Figure 5). If we consider the node-to-node oscillation, its derivative is an odd function, the inner product of which with the test function is identically zero. This is a solution!

Now, if the test function includes both odd and even components, this mode will no longer be a solution. In fact, if we weight the test function upstream, these oscillations are damped; weighting downstream amplifies them. A common approach is to use a test function, ψ , weighted as follows,

$$\psi_i = \phi_i + \alpha \Delta x \frac{|U_0|}{U_0} \frac{d\phi_i}{dx} \quad (41)$$

where α is a weighting parameter.

Here the spatial derivative supplies the odd component to the test function. The resulting discrete solution using this test function is

$$\left(\psi_i, U_0 \frac{\partial(\Sigma \phi_j C_j)}{\partial X} \right) = 0, \text{ for each } i \quad (42)$$

from which the numerical roots may be calculated by

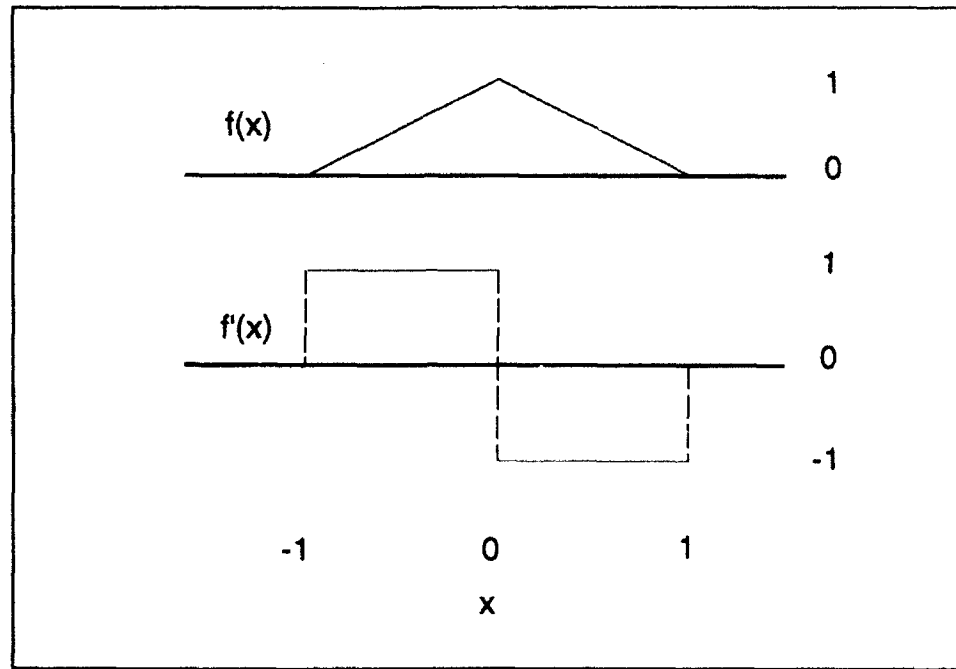


Figure 5. The node-to-node oscillation and slope over a typical grid patch

$$\frac{1}{2} U_0 (\rho^2 - 1) - \alpha |U_0| (\rho - 1)^2 = 0 \quad (43)$$

the roots of which are then

$$\rho = 1, \frac{\alpha + \frac{1}{2}}{\alpha - \frac{1}{2}} \quad (44)$$

If $\alpha \geq 1/2$ we will have no negative roots and therefore should not have a node-to-node oscillation. This spurious root that we damp by increasing the coefficient α is driven by some abrupt change, most notably when some discontinuity is required in the equations due to the imposition of boundary conditions. It is more precise in a smooth region for smaller α .

The situation is more complex for the shallow-water equations, since we have a coupled set of partial differential equations. We shall demonstrate the method used in this model by showing how it relates in 1-D to the decoupled linearized equations using the Riemann Invariants as the routed variables.

The 1-D shallow-water equations in conservative form may be written

$$\frac{\partial Q}{\partial t} + \frac{\partial}{\partial X} F(Q) = 0 \quad (45)$$

where

$$Q = \begin{Bmatrix} h \\ p \end{Bmatrix}$$

$$p = Uh$$

$$F(Q) = \begin{Bmatrix} p \\ \frac{p^2}{h} + \frac{1}{2} gh^2 \end{Bmatrix}$$

If we consider the linearized system with the Jacobian matrix A as a constant, the nonconservative shallow-water equations may be written as

$$\frac{\partial Q}{\partial t} + A \frac{\partial Q}{\partial X} = 0 \quad (46)$$

where

$$A = \begin{bmatrix} 0 & 1 \\ C_0^2 - U_0^2 & -2U_0 \end{bmatrix}, \quad C_0 = \sqrt{gh_0}$$

and the subscript 0 indicates a constant value.

We may select the matrix P such that

$$P^{-1} \Lambda P = A$$

where Λ is the matrix of eigenvalues of A , and P and P^{-1} are composed of the eigenvectors.

$$\Lambda = \begin{bmatrix} \lambda_1 & 0 \\ 0 & \lambda_2 \end{bmatrix} = \begin{bmatrix} U_0 + C_0 & 0 \\ 0 & U_0 - C_0 \end{bmatrix}$$

If we define a new set of variables (the Riemann Invariants) as

$$T = PQ$$

we may write the shallow-water equations as two decoupled equations

$$\frac{\partial T}{\partial t} + \Lambda \frac{\partial T}{\partial X} = 0 \quad (47)$$

for which it is apparent that we can propose a test function as

$$I\psi = I\phi + \alpha \Delta X |\Lambda| \Lambda^{-1} \frac{\partial \phi}{\partial X} \quad (48)$$

which can be returned to the original system in terms of the variable Q as

$$I\psi = I\phi + \alpha \Delta X P^{-1} |\Lambda| \Lambda^{-1} P \frac{\partial \phi}{\partial X} \quad (49)$$

The size and direction of the added odd function is then based upon the magnitude and direction of the characteristics.

This particular test function is weighted upstream along characteristics. This is a concept like that developed in the finite difference method of Courant, Isaacson, and Rees (1952) for one-sided differences. These ideas were expanded to more general problems by Moretti (1979) and Gabutti (1983) as split-coefficient matrix methods and by the generalized flux vector splitting proposed by Steger and Warming (1981). In the finite elements community, instead of one-sided differences the test function is weighted upstream. This particular method in 1-D is equivalent to the SUPG scheme of Hughes and Brooks (1982) and similar to the form proposed by Dendy (1974). Examples of this approach in the open-channel environment are for the generalized shallow-water equations in 1-D in Berger and Winant (1991) and for 2-D in Berger (1992). A 1-D St. Venant application is given by Hicks and Steffler (1992).

If we analyze this approach on a uniform grid, we find the following roots

$$\rho = 1, \frac{\alpha \lambda_1 + \frac{1}{2}}{\alpha \lambda_1 - \frac{1}{2}}, \frac{\alpha \lambda_2 + \frac{1}{2}}{\alpha \lambda_2 - \frac{1}{2}} \quad (50)$$

Again if $\alpha \geq 1/2$, all roots are non-negative and so node-to-node oscillations are damped. In 2-D we follow a similar procedure.

The particular approach to numerical simulation chosen here is a Petrov-Galerkin finite element method applied to the shallow-water equations.

For the shallow-water equations in conservative form (Equation 1), the Petrov-Galerkin test function ψ_i is defined as

$$\psi_i I = \phi_i I + \alpha \left(\Delta x \frac{\partial \phi_i}{\partial x} \hat{A} + \Delta y \frac{\partial \phi_i}{\partial y} \hat{B} \right) \quad (51)$$

where

α = dimensionless number between 0 and 0.5

ϕ = linear basis function

In the manner of Katopodes (1986), we choose

$$\Delta x = 2 \left[\left(\frac{\partial x}{\partial \xi} \right)^2 + \left(\frac{\partial x}{\partial \eta} \right)^2 \right]^{1/2}$$

$$\Delta y = 2 \left[\left(\frac{\partial y}{\partial \xi} \right)^2 + \left(\frac{\partial y}{\partial \eta} \right)^2 \right]^{1/2}$$

ξ and η are the local coordinates defined from -1 to 1.

To find \hat{A} consider the following:

$$A = \frac{\partial F_x(Q)}{\partial Q}$$

$$P^{-1} \Lambda P = A$$

where $\Lambda = \Gamma \lambda$ is the matrix of eigenvalues of A and P and P^{-1} are made up of the right and left eigenvectors.

$$\hat{A} = P^{-1} \hat{\Lambda} P$$

where

$$\hat{\Lambda} = \begin{bmatrix} \frac{\lambda_1}{(\lambda_1^2 + V^2)^{1/2}} & 0 & 0 \\ 0 & \frac{\lambda_2}{(\lambda_2^2 + V^2)^{1/2}} & 0 \\ 0 & 0 & \frac{\lambda_3}{(\lambda_3^2 + V^2)^{1/2}} \end{bmatrix}$$

and

$$\lambda_1 = U + C$$

$$\lambda_2 = U - C$$

$$\lambda_3 = U$$

$$C = (gh)^{1/2}$$

A similar operation may be performed to define \hat{B} .

Shock Capturing

In the section, "Shock equations," in Chapter 1 we have shown that unless there is a discontinuity in depth, mechanical energy will be conserved in the shallow-water equations (with no friction or diffusion). So the obvious question is what happens in a numerical scheme in which the depth is approximated as C^0 ; i.e., it is continuous. We are only enforcing mass and momentum, but we are implicitly enforcing energy conservation. This is the result that the Galerkin approach will give using C^0 depth approximation. The result is that while mass and momentum conservation are enforced over our discrete model, energy is also conserved by including the spurious node-to-node mode we discussed. Since energy involves V^2 terms and momentum only V , both can be satisfied in a weighted average sense over the region included in the test function. This is due to

$$\int_{\Omega} V^2 d\Omega \approx \int_{\Omega} \bar{V}^2 d\Omega \quad (52)$$

where the term \bar{V} means the average value.

Basically, energy is "hidden" from the numerical scheme in the shortest wavelength since the model cannot "see" this in enforcing momentum conservation. So what we need is a scheme that damps this shortest wavelength and thus dissipates the energy. As we demonstrated in the previous section, this is precisely what our scheme does. Therefore, the Petrov-Galerkin scheme we are using to address advection-dominated flow is a good scheme for shock capturing as well. The scheme dissipates energy at the short wavelengths.

We have shown that when a shock is encountered, the weak solution of the shallow-water equations must lose mechanical energy. Some of this energy loss is analogous to a physical hydraulic system losing energy to heat, particle rotation, deformation of the bed, etc; but much of it is, in fact, simply the energy being transferred into vertical motion. And since vertical motion is not included in the shallow-water equations, it is lost. This apparent energy loss can be used to our advantage.

We would like to apply a high value of α , say 0.5, only in regions in which it is needed, since a lower value is more precise. Therefore, we wish to construct a trigger mechanism which can detect shocks and increase α automatically. The method we employ detects energy variation for each element and flags those elements which have a high variation as needing a larger value of α for shock capturing. Note that this would work even in a Galerkin scheme since this trigger is concerned with energy variation on an element basis and the Galerkin method would enforce energy conservation over a test function (which includes several elements).

The shock capturing is implemented when Equation 53 is true

$$|Ts_i| > \gamma \quad (53)$$

where

$$Ts_i = \frac{ED_i - \bar{E}}{S}$$

where ED_i , the element energy deviation, is calculated by

$$ED_i = \frac{\left[\int_{\Omega_i} (E - \bar{E}_i)^2 d\Omega \right]^{1/2}}{a_i}$$

where

Ω_i = element i

E = mechanical energy

a_i = area of element i

and \bar{E}_i , the average energy of element i , is calculated by

$$\bar{E}^i = \frac{\int_{\Omega_i} E d\Omega}{a_i}$$

and

\bar{E} = the average element energy over the entire grid

S = the standard deviation of all ED_i

Through trial a value of γ of 1.0 was chosen.

An apparent limitation of this method is that it relies upon how the elemental deviation compares with that of all the other elements of the grid. If a problem contains no shocks, it would still select the worst elements and raise the value of α . Conversely, if the domain contains numerous shocks, it might not catch all of them. Perhaps some ratio of (ED_i/\bar{E}) might be meaningful, and should be addressed in future studies.

3 Testing

The testing of this scheme and model behavior was undertaken in stages. These progress from what is essentially a 1-D test for shock speed which can be determined analytically, to a 2-D dam break type problem comparison with flume data, to more general 2-D geometry comparison of supercritical transition in a flume but for steady state. This series tests the model against the analytic results of the shallow-water equations for very limited geometry, and progresses to more general geometry with the limitation of the shallow-water equations in reproducing actual flow problems. The applicability of the shallow-water equations to these flume conditions is not so important in this study (since it is interested in shock capturing), but is important for model application in open-channel hydraulics.

The first test is performed to determine the comparison of model versus analytic shock speed in a long straight flume. Shock speed will be poorly modeled if the numerical scheme is handled improperly. The analytic and model tests are performed in which the flow is initially constant and supercritical; then the lower boundary is shut so that a wall of water is formed that propagates upstream. This speed can be determined analytically, and a comparison is made between the analytic speed and the model predictions for a range of resolutions and time-step sizes.

The second case is a comparison to a flume data set reported in Bell, Elliot, and Chaudhry (1992) which is analogous to a dam break problem. Here the shock is in a horseshoe-shaped channel and the comparison is to actual flume data. The comparisons are made to the water surface heights and timing of the shock passage.

The final case is a steady-state comparison to flume data reported in Ippen and Dawson (1951). Here a lateral transition under supercritical flow conditions generates a field of oblique jumps. The model comparison is made to these conditions, which is a more general 2-D domain than previous tests.

Case 1: Analytic Shock Speed

The shock speed for the shallow-water equations given simple 1-D geometry can be determined analytically. These are the Rankine-Hugoniot relations shown in Equations 5 and 9. This provides a direct comparison with the model shock speed without relying upon hydraulic flume data, for which discrepancy will be due to the hydrostatic assumption made in the shallow-water equations. Instead we have a direct way of evaluating the numerical scheme alone. As spatial and temporal resolution increase, the numerical shock speed should converge to the analytic speed. The test consists of setting a supercritical flow in a long channel, closing the downstream end, and calculating the speed of the jump that forms and propagates upstream. The initial conditions for this test case are shown in Table 1. The test conditions are shown in Table 2. The term α_f indicates the

Table 1
Initial Conditions for the Analytic Shock Speed Case

Condition	Value
depth	0.1 m
U	$(0.3)^{1/2}$
g	4 m/s ²

Table 2
Test Conditions for the Analytic Shock Speed Case

Condition	Value
α_f	1.0, 1.5
α, α_s	0.25, 0.50
n	0.0
ν, ν_s	0.0, 0.0

method applied to the temporal derivative, 1.0 is first-order backward, and 1.5 is second-order backward. The subscript s indicates the value in the shock vicinity. The α and α_s are the weighting of the Petrov-Galerkin contribution throughout the domain and in the shock vicinity, respectively. With Manning's n and viscosity of 0.0 there is no dissipation in the shallow-water equations.

Figures 6-8 and 9-11 show the center-line profile over time of these tests for $\alpha_f = 1.0$ and for $\Delta X = 0.4$ and 0.8 m, respectively. These plots represent the center-line depth profile over time in a perspective view. The vertical axis is the flow depth, the horizontal axis is time, and the axis that appears to be into the page is the distance along the channel. From this one can see that as

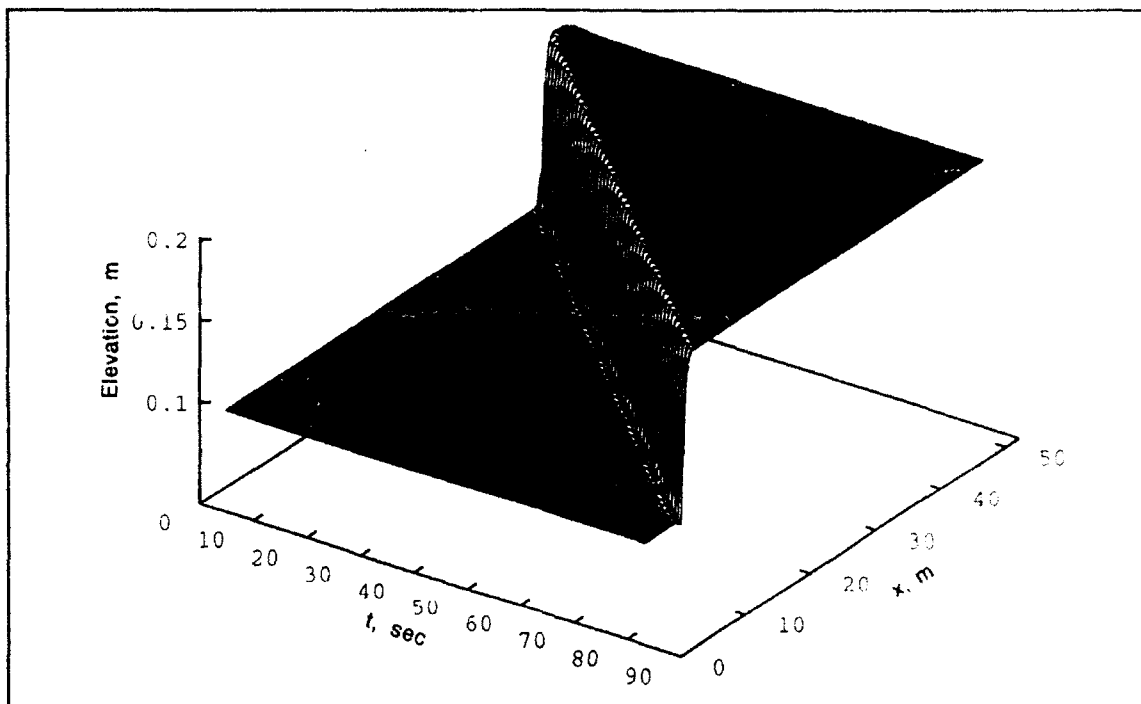


Figure 6. Time-history of center-line water surface elevation profiles; $\alpha_t = 1.0$, $\Delta x = 0.4$ m, $\Delta t = 0.4$ sec

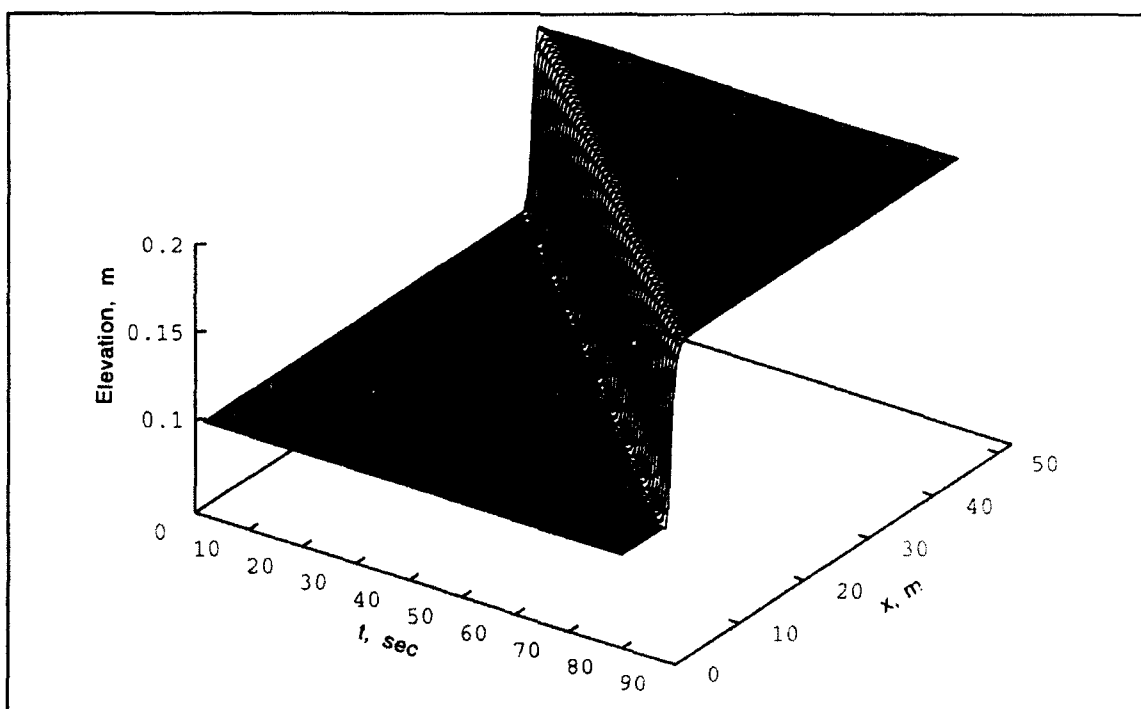


Figure 7. Time-history of center-line water surface elevation profiles; $\alpha_t = 1.0$, $\Delta x = 0.4$ m, $\Delta t = 0.8$ sec

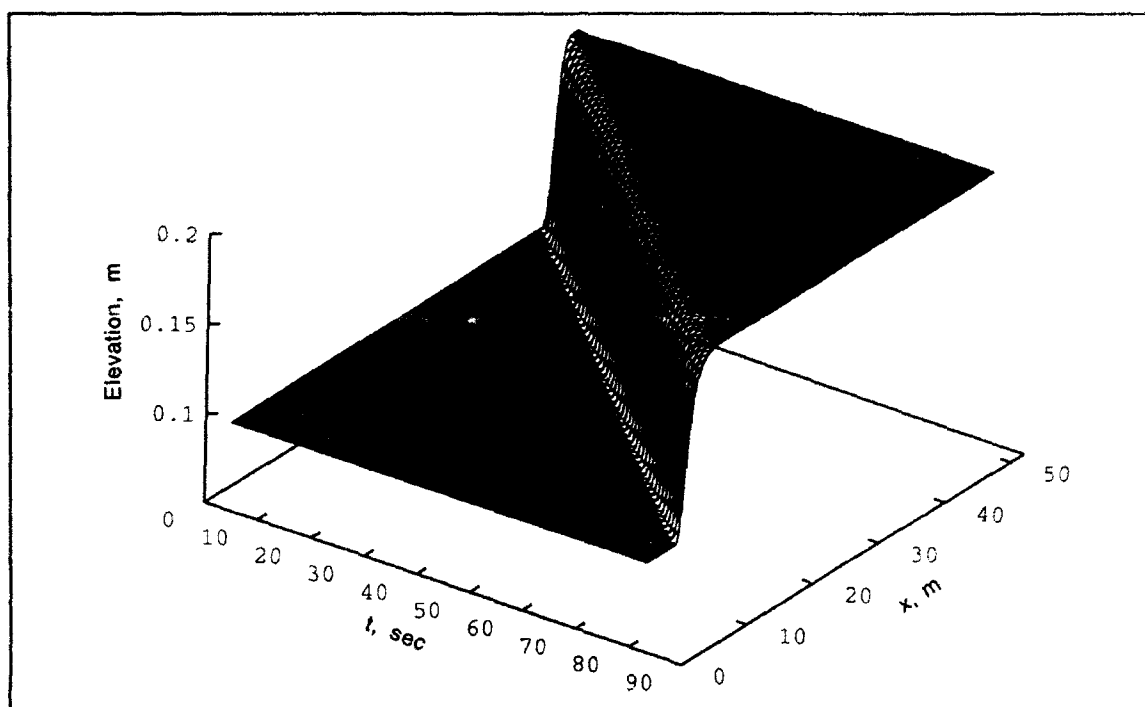


Figure 8. Time-history of center-line water surface elevation profiles; $\alpha_t = 1.0$, $\Delta x = 0.4$ m, $\Delta t = 1.6$ sec

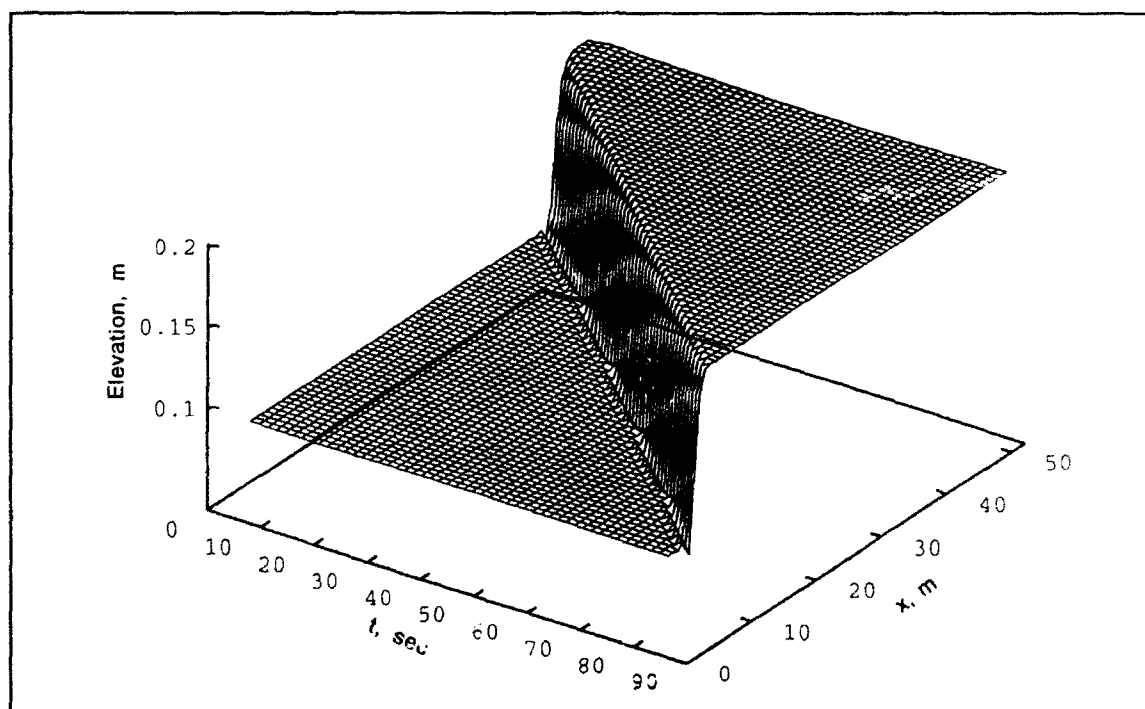


Figure 9. Time-history of center-line water surface elevation profiles; $\alpha_t = 1.0$, $\Delta x = 0.8$ m, $\Delta t = 0.8$ sec

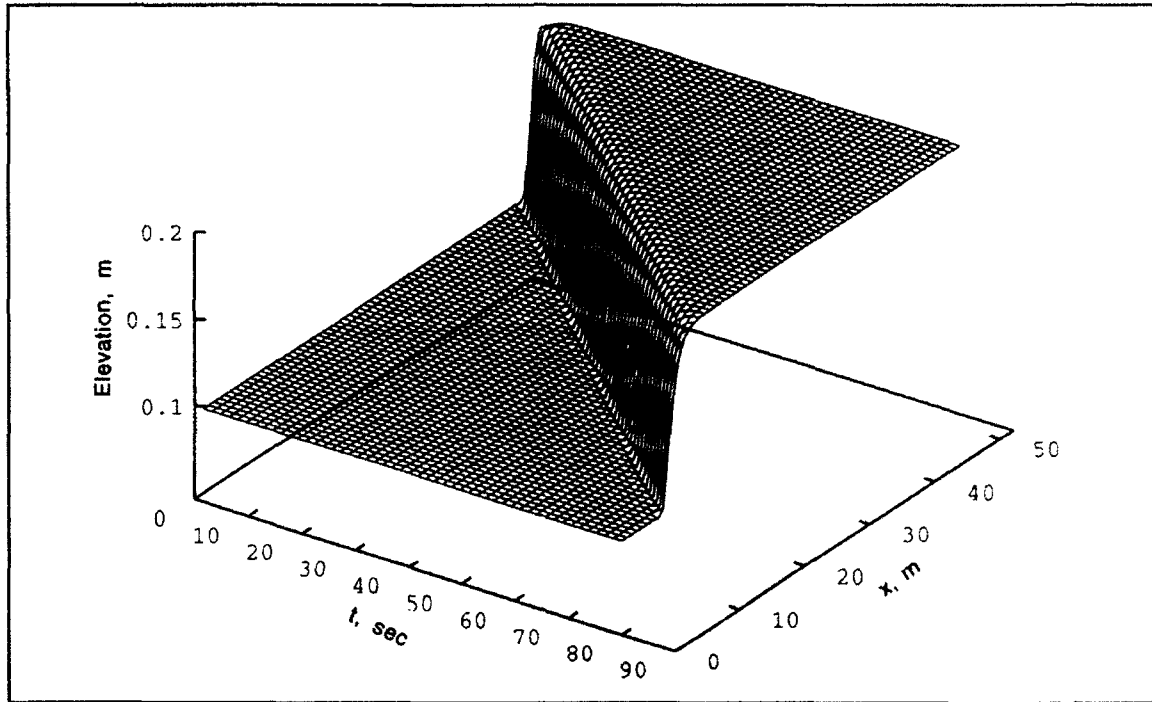


Figure 10. Time-history of center-line water surface elevation profiles; $\alpha_t = 1.0$, $\Delta x = 0.8$ m, $\Delta t = 1.6$ sec

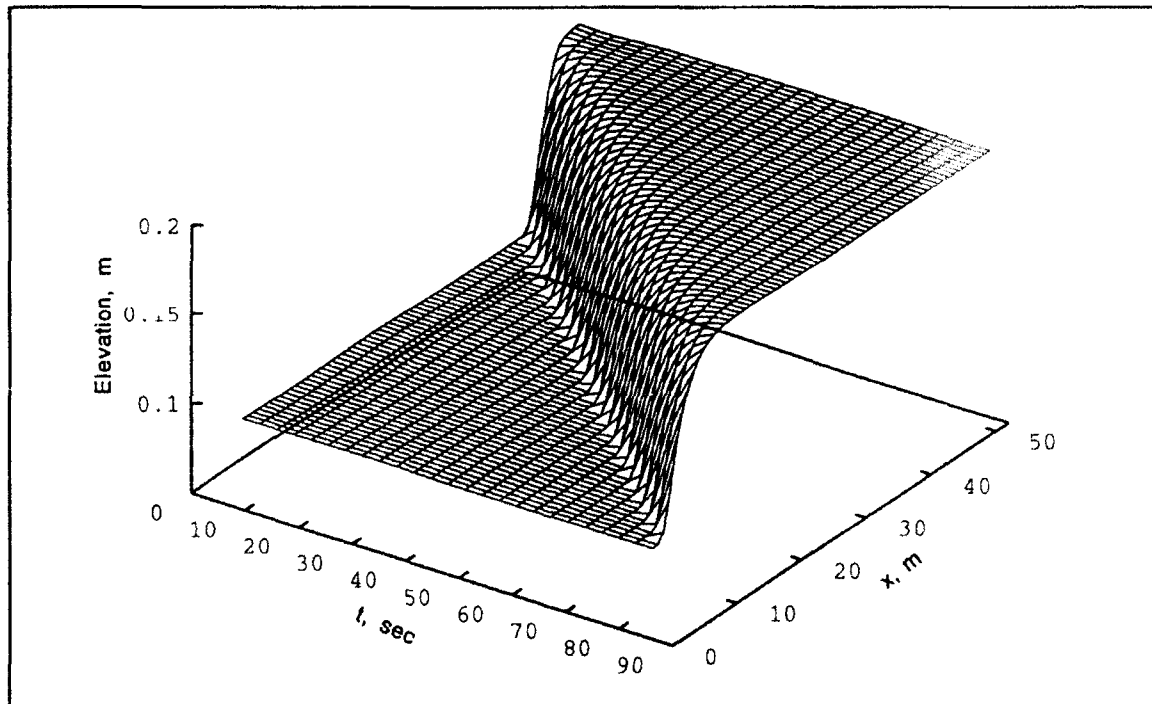


Figure 11. Time-history of center-line water surface elevation profiles; $\alpha_t = 1.0$, $\Delta x = 0.8$ m, $\Delta t = 3.2$ sec

one moves over time, the center-line profile shock moves upstream. It is apparent that as the spatial and temporal resolution improve, the shock becomes steeper. The shock is fairly consistently spread over three or four elements; and so as the element size is reduced, the resulting shock is steeper. The $x-t$ slope of the shock indicates the shock speed. Any bending would indicate that the speed changed over time, which should not be the case. The upper elevation is precisely 0.2 m, which is correct. There is no overshoot of the jump, though there is some undershoot when C_s is less than 1. C_s is the product of the analytic shock speed and the ratio of time-step length to element length. A C_s value of 1 indicates that the shock should move 1 element length in 1 time-step.

Figures 12 and 13 show the error in calculated speed and the relative error in calculated speed, respectively. These are for $\Delta X = 0.4, 0.8$ and 1.0 m which is reflected in the Grid Resolution Number defined as $\Delta X/\Delta h$. Here h is the depth and Δh is the analytic depth difference across the shock, 0.1 m. The error was as small as was detectable by the technique for measurement of speed at $\Delta X = 0.4$ m so there was no need to go to smaller grid spacing. Values of C_s less than 1 appear to lag the analytic shock and C_s greater than 1 leads the analytic shock. With the largest C_s the calculated shock speed is greater than the analytic by at most 0.0034 m/sec which is only 0.6 percent too fast. As resolution is improved the solution appears to converge to the analytic speed.

Figures 14-16 and 17-19 are the center-line profile histories for $\alpha_f = 1.5$ and for $\Delta X = 0.4$ and 0.8 m, respectively. It is apparent that the lower dissipation from this second-order scheme allows an oscillation which is most notable upstream of the jump for larger values of C_s . But as C_s decreases, there is an undershoot in front of the shock. The slope of the $x-t$ line along the top of the shock has a significant bend early in the high C_s simulations. The speed is too slow here.

Now consider the associated Figures 20 and 21 for error in calculated shock speed and relative error in calculated speed. The error is actually worse than for the first-order scheme. This is due primarily to the slow speed early in the simulation; if this is dropped by using only the last 50 seconds of simulation, the relative error is only 0.6 percent slower than analytic. Once again, as the resolution improves, the solution converges to the proper solution.

Case 2: Dam Break

This second case is a comparison to hydraulic flume results reported in Bell, Elliot, and Chaudhry (1992). A plan view of the flume facility is shown in Figure 22. The flume was constructed of Plexiglas and simulates a dam break through a horseshoe bend. This is a more general comparison than Case 1. Here the problem is truly 2-D and we now are comparing to hydraulic flume results, so we must take into consideration the limitations of the shallow-water equations themselves. Initially, the reservoir has an elevation of 0.1898 m relative to the channel bed; the channel itself is at a depth (and elevation) of 0.0762 m. The velocity is zero and then the dam is removed. The surge location and height were recorded at several stations, and our model is compared at three of these, at stations 4, 6, and 8. Station 4 is 6.00 m from the dam along the channel center-line in the center of the bend, station 6 is 7.62 m from the dam near the conclusion of the bend, and station 8 is 9.97 m from the dam in a straight reach. The model specified parameters are shown in Table 3.

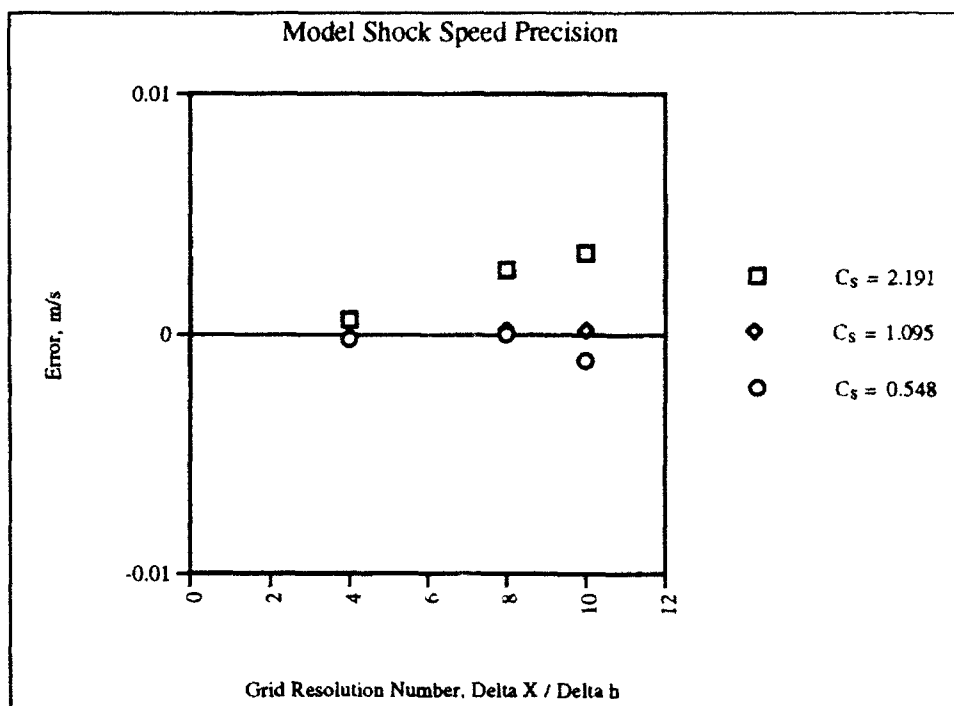


Figure 12. Error in model shock speed with grid refinement for $\alpha_t = 1.0$

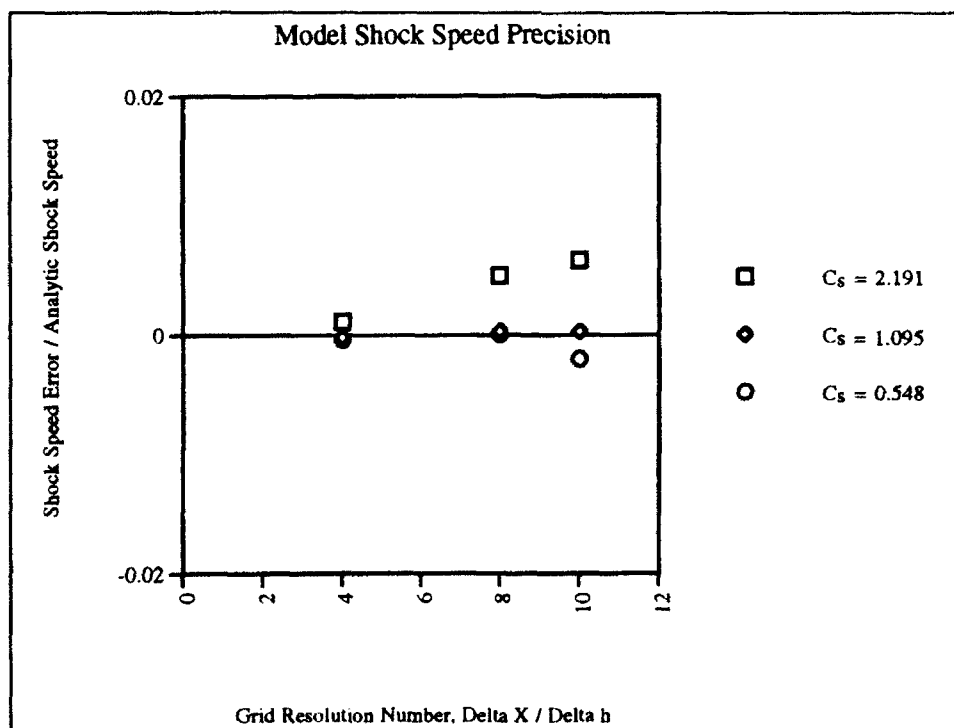


Figure 13. Relative error in model shock speed with grid refinement for $\alpha_t = 1.0$

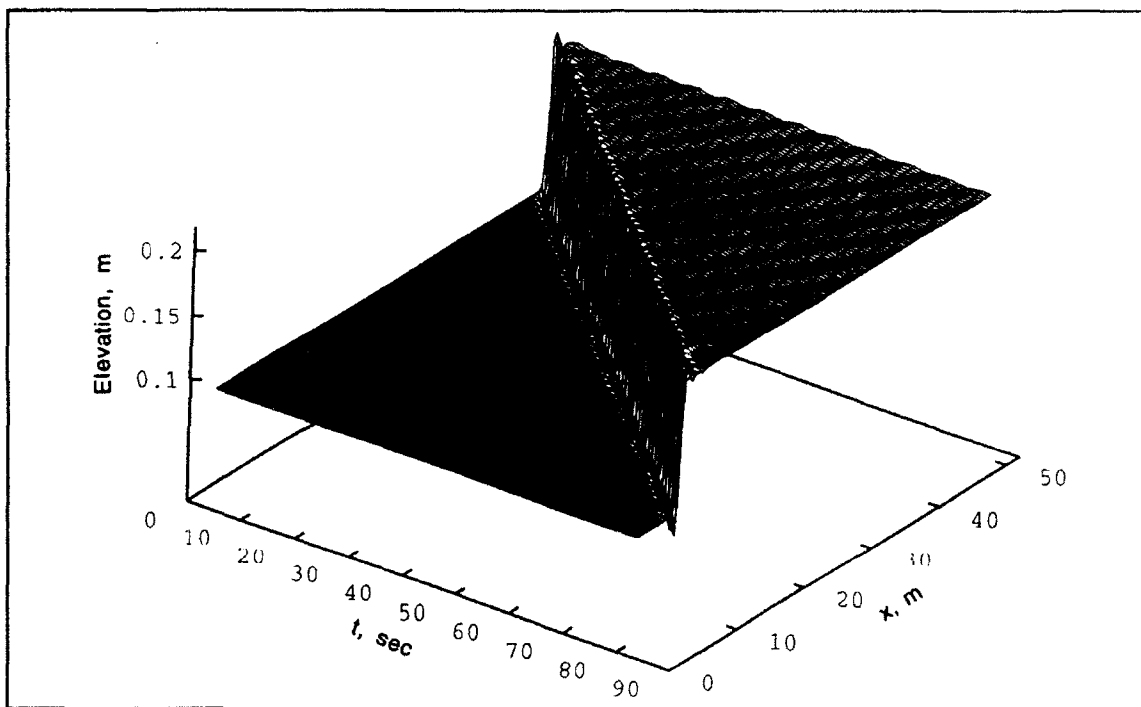


Figure 14. Time-history of center-line water surface elevation profiles; $\alpha_t = 1.5$, $\Delta x = 0.4$ m, $\Delta t = 0.4$ sec

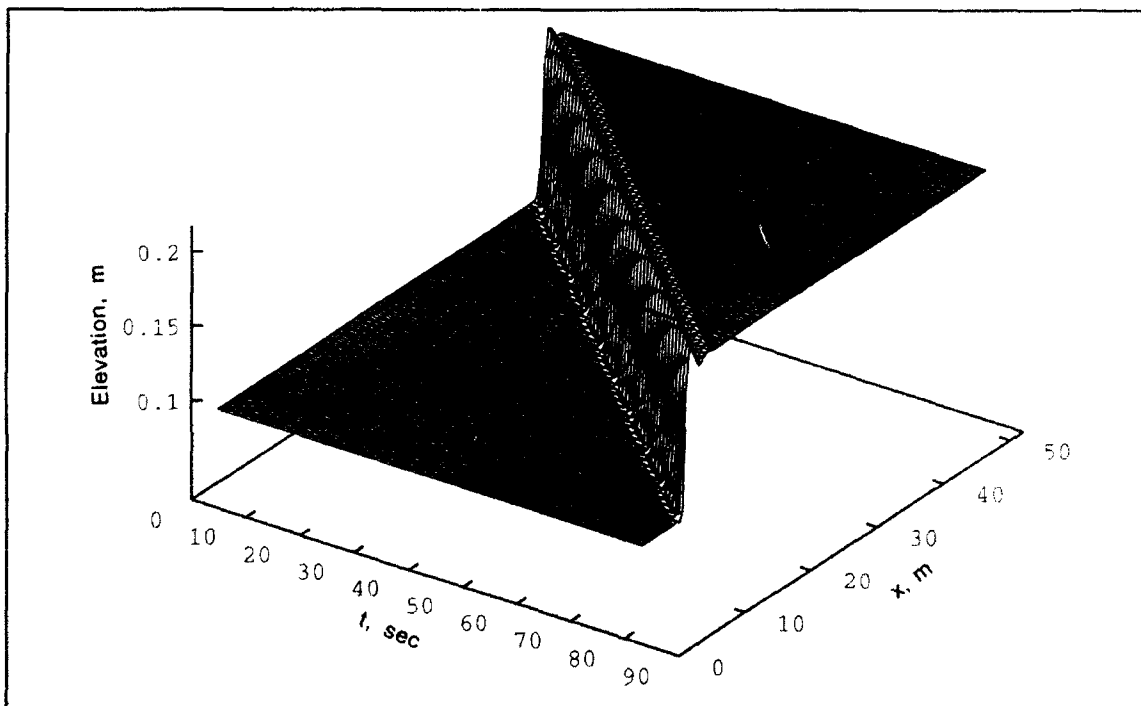


Figure 15. Time-history of center-line water surface elevation profiles; $\alpha_t = 1.5$, $\Delta x = 0.4$ m, $\Delta t = 0.8$ sec

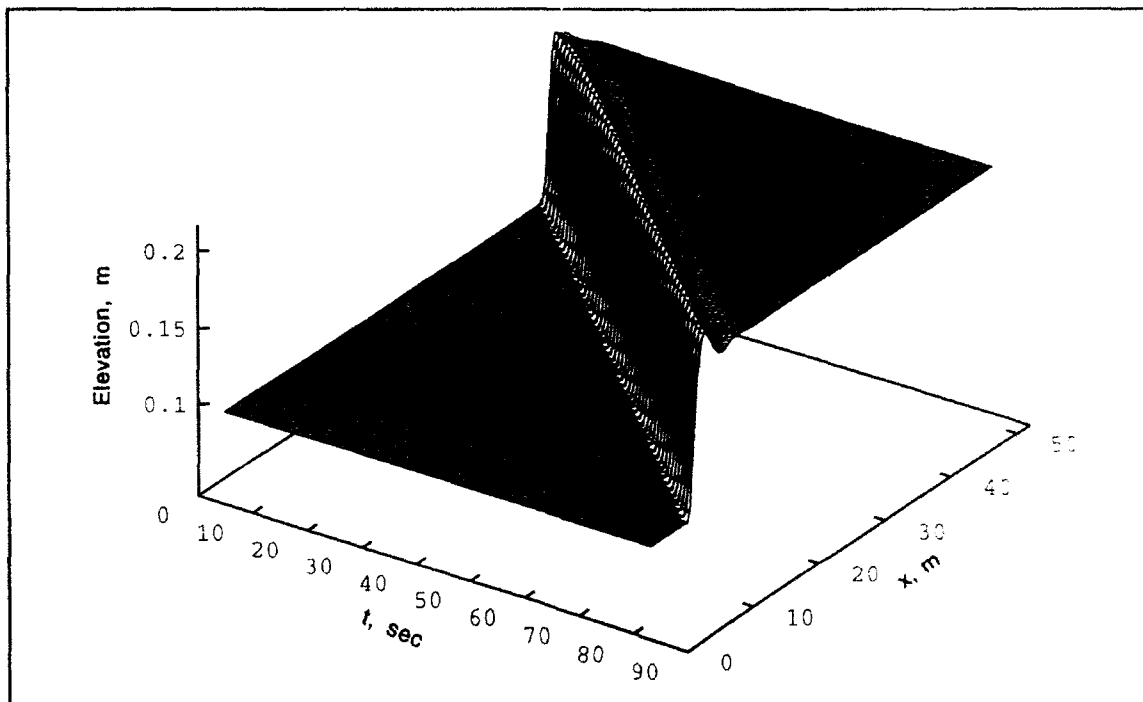


Figure 16. Time-history of center-line water surface elevation profiles; $\alpha_t = 1.5$, $\Delta x = 0.4$ m, $\Delta t = 1.6$ sec

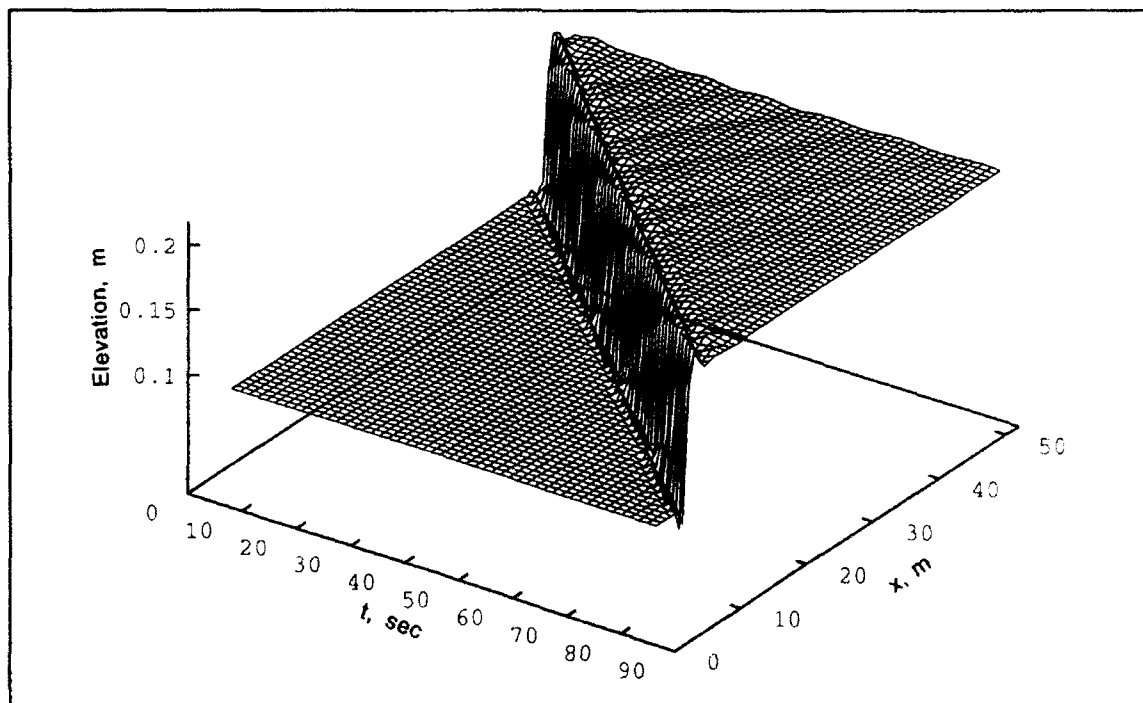


Figure 17. Time-history of center-line water surface elevation profiles; $\alpha_t = 1.5$, $\Delta x = 0.8$ m, $\Delta t = 0.8$ sec

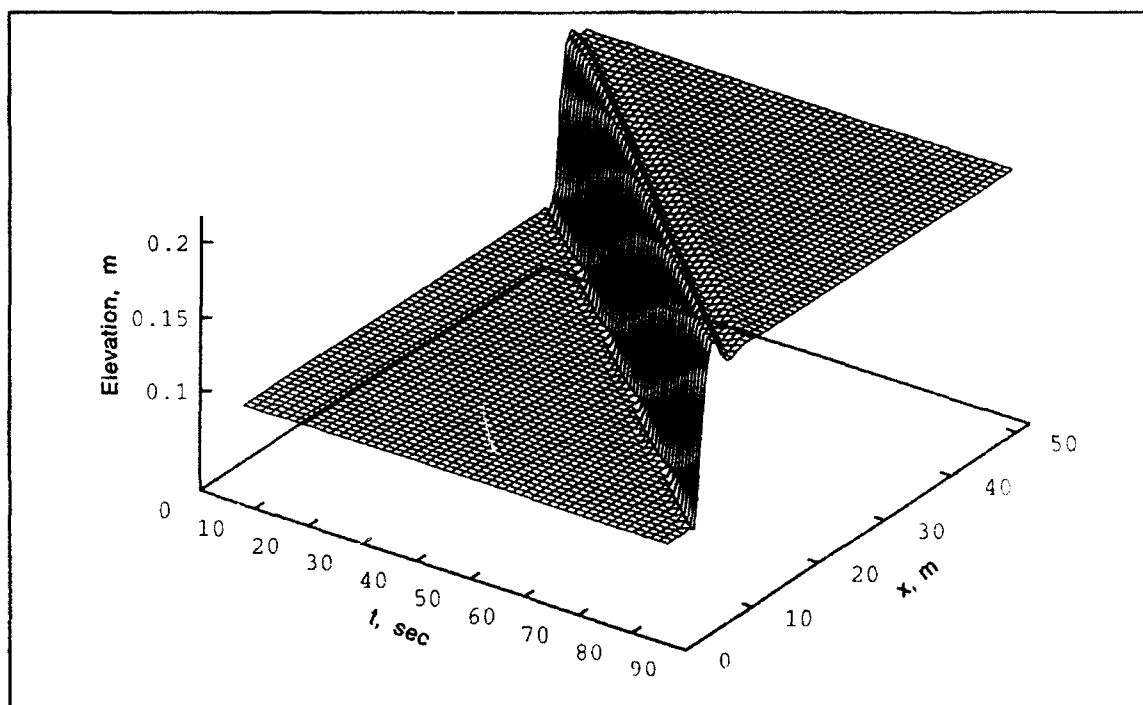


Figure 18. Time-history of center-line water surface elevation profiles; $\alpha_t = 1.5$, $\Delta x = 0.8$ m, $\Delta t = 1.6$ sec

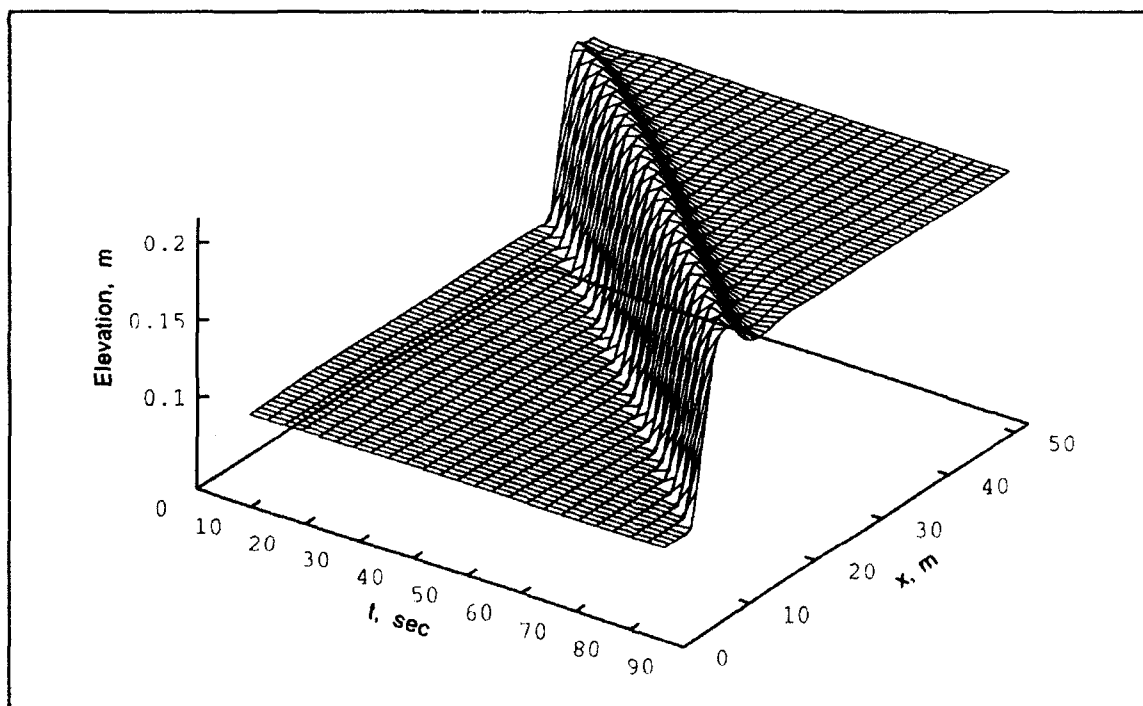


Figure 19. Time-history of center-line water surface elevation profiles; $\alpha_t = 1.5$, $\Delta x = 0.8$ m, $\Delta t = 3.2$ sec

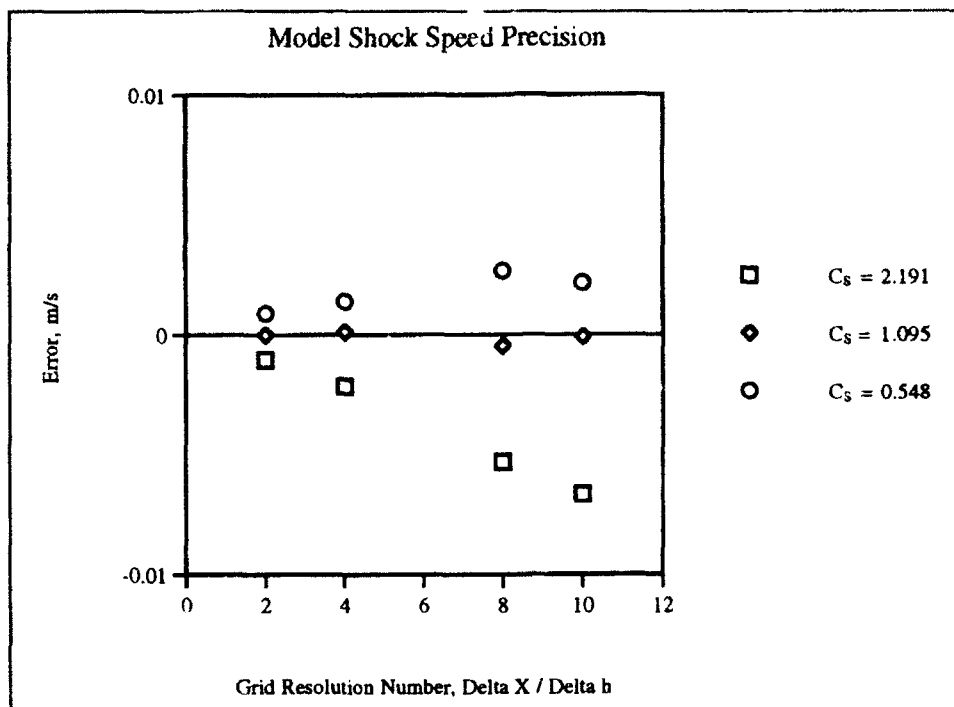


Figure 20. Error in model shock speed with grid refinement for $\alpha_t = 1.5$

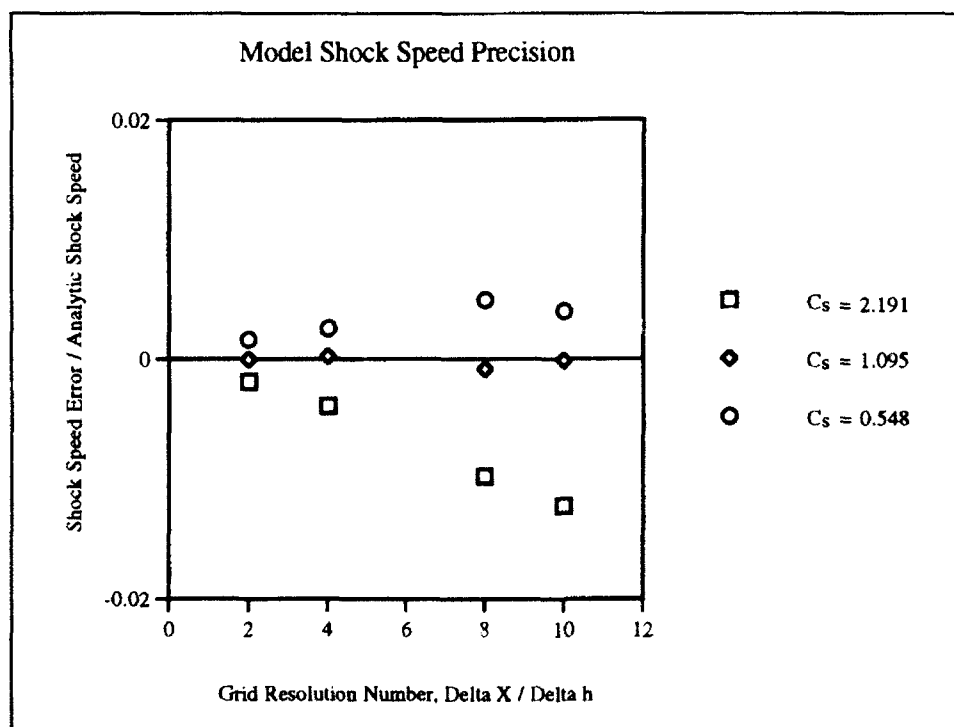


Figure 21. Relative error in model shock speed with grid refinement for $\alpha_t = 1.5$

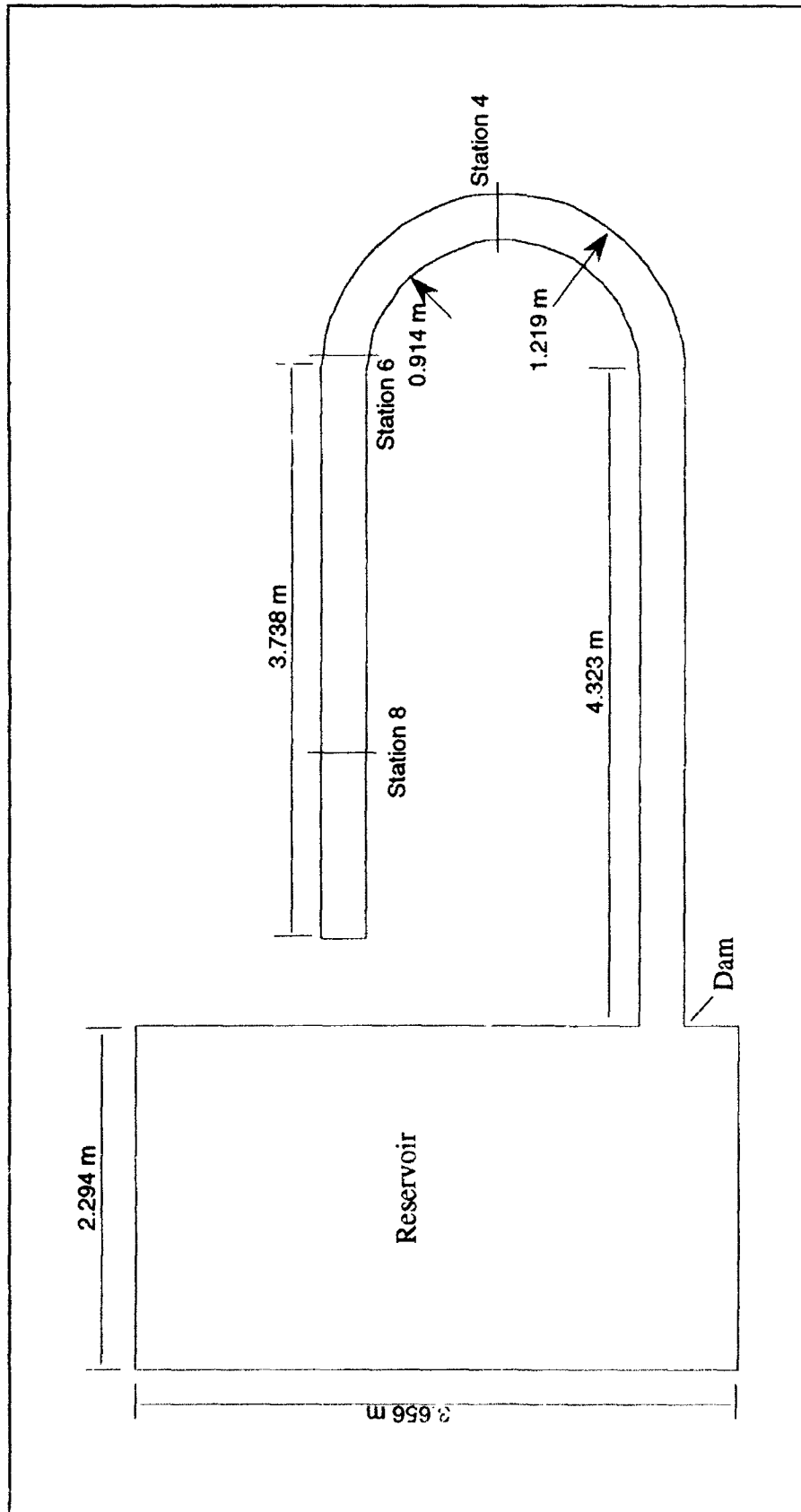


Figure 22. Plan view of dam break test flume and stations (after Bell, Elliot, and Chaudhry 1992)

Table 3 Test Conditions For The Dam Break Case	
Condition	Value
α_l	1.0, 1.5
α, α_s	0.25, 0.50
n	0.009
v, v_s	0.001, 0.01 m ² /sec
g	9.802 m/sec ²
Δt	0.05 sec

The numerical grid is shown in Figure 23, and contains 698 elements and 811 nodes. This grid was reached by increasing the resolution until the results no longer changed. The most critical reach is in the region of the contraction near the dam breach. The basic element length in the channel is 0.1 m and there are five elements across the channel width. For the smooth channel case, Bell, Elliot, and Chaudhry (1992) used a 1-D calculation to estimate the Manning's n to be 0.016 but experience at the Waterways Experiment Station suggests that this value should actually be 0.009, which seems more reasonable.

The test results for stations 4, 6 and 8 are shown in Figures 24-26. Here the time-history of the water elevation is shown for the inside and outside of the channel for both the numerical model (at α_l of 1.0 and 1.5) and the flume. The inside wall is designated by squares and the outside by diamonds. Of particular importance is the arrival time of the shock front. At station 4 the numerical prediction of arrival time using α_l of 1.0 is about 3.4 sec which appears to be about 0.05 sec sooner than for the flume. This is roughly 1-2 percent fast. For α_l of 1.5 the time of arrival is 3.55 sec which is about 0.1 sec late (3 percent). At station 6 both flume and numerical model arrival times for α_l of 1.0 were about 4.3 sec and for station 8 the numerical model is 5.6 sec and the flume is 5.65 to 5.8 sec. With α_l set at 1.5 the time of arrival is late by about 0.2 and 0.15 sec at stations 6 and 8, respectively. The flume at stations 6 and 8 has a earlier arrival time for the outer wave compared to the inner wave. The numerical model does not show this. In comparing the water elevations between the flume and the numerical model, it is apparent that the flume results show a more rapid rise. The numerical model is smeared somewhat in time likely as a result of the first-order temporal derivative calculation of α_l of 1.0. The numerical model with α_l set at 1.5 shows the overshoot that was demonstrated in Case 1. This is likely a numerical artifact and not based upon physics even though this looks much like the flume results. The surge elevations predicted by the numerical model are fairly close if one notices that the initial elevation of the flume data is supposed to be 0.0762 m and it appears to be recorded as much as 0.015 m higher at some gages. Since the velocity is initially zero then all of these readings should have been 0.0762 m and all should be adjusted to match this initial elevation.

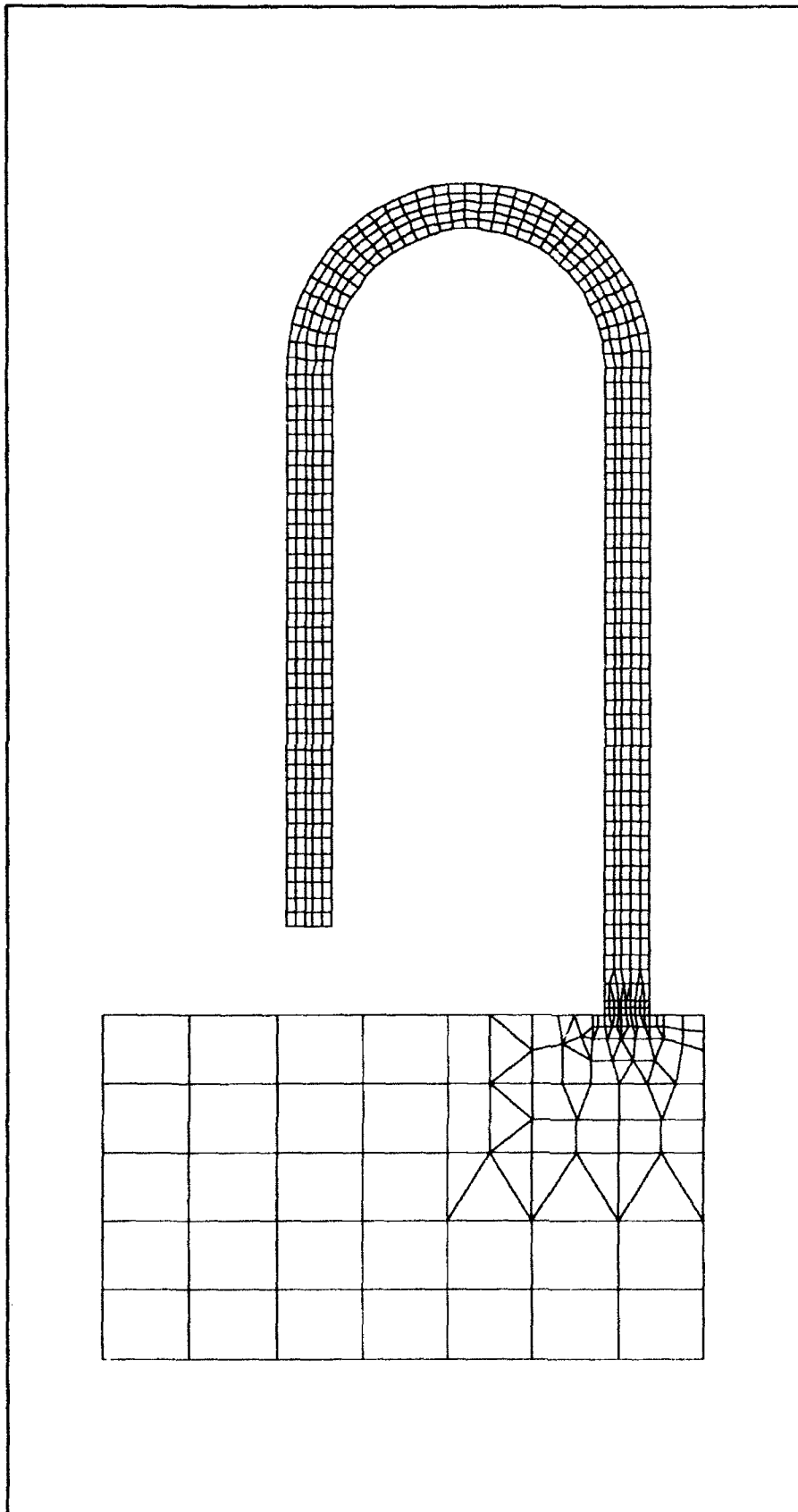


Figure 23. Numerical model computational mesh for the dam break case

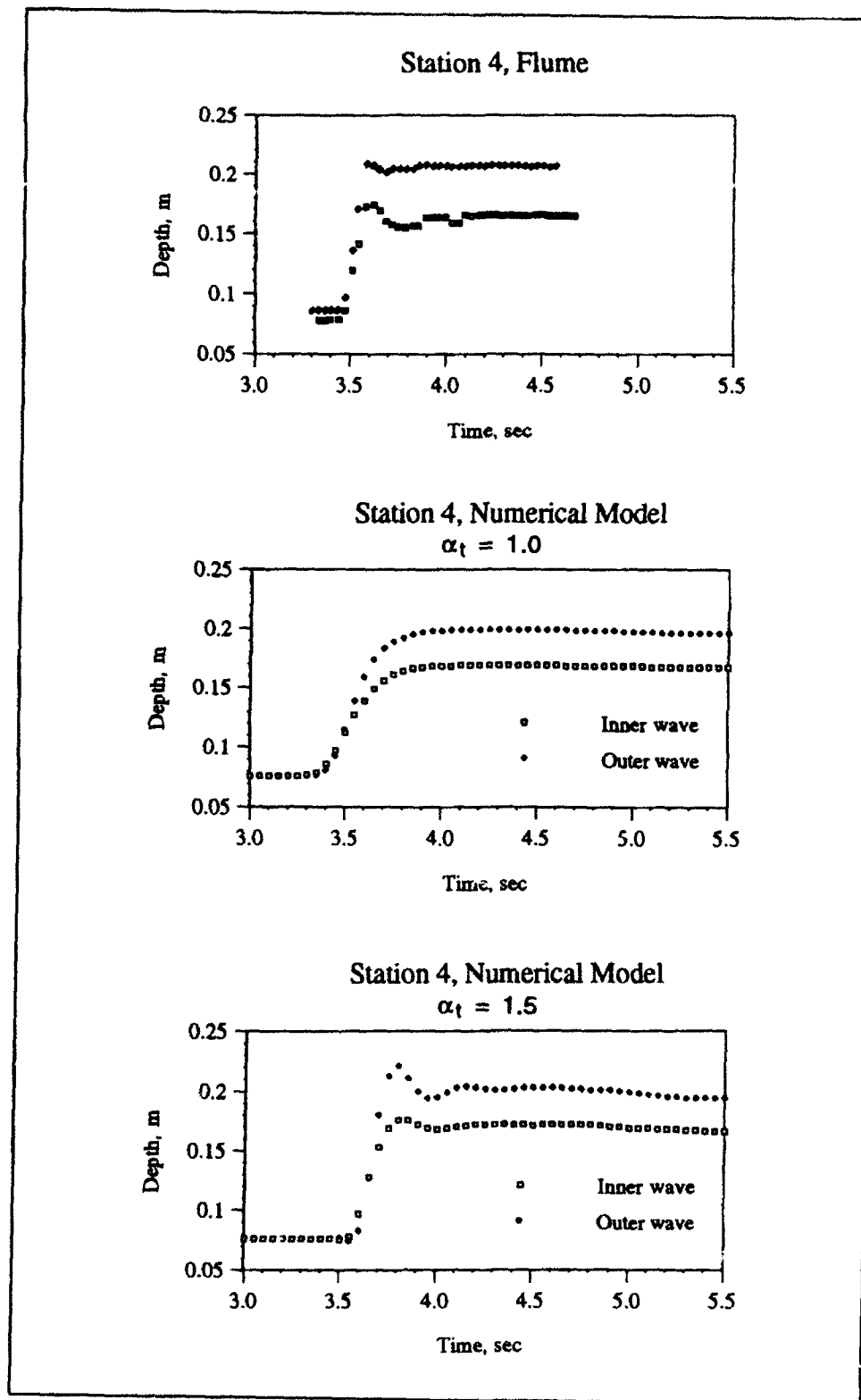


Figure 24. Flume and numerical model depth histories for station 4

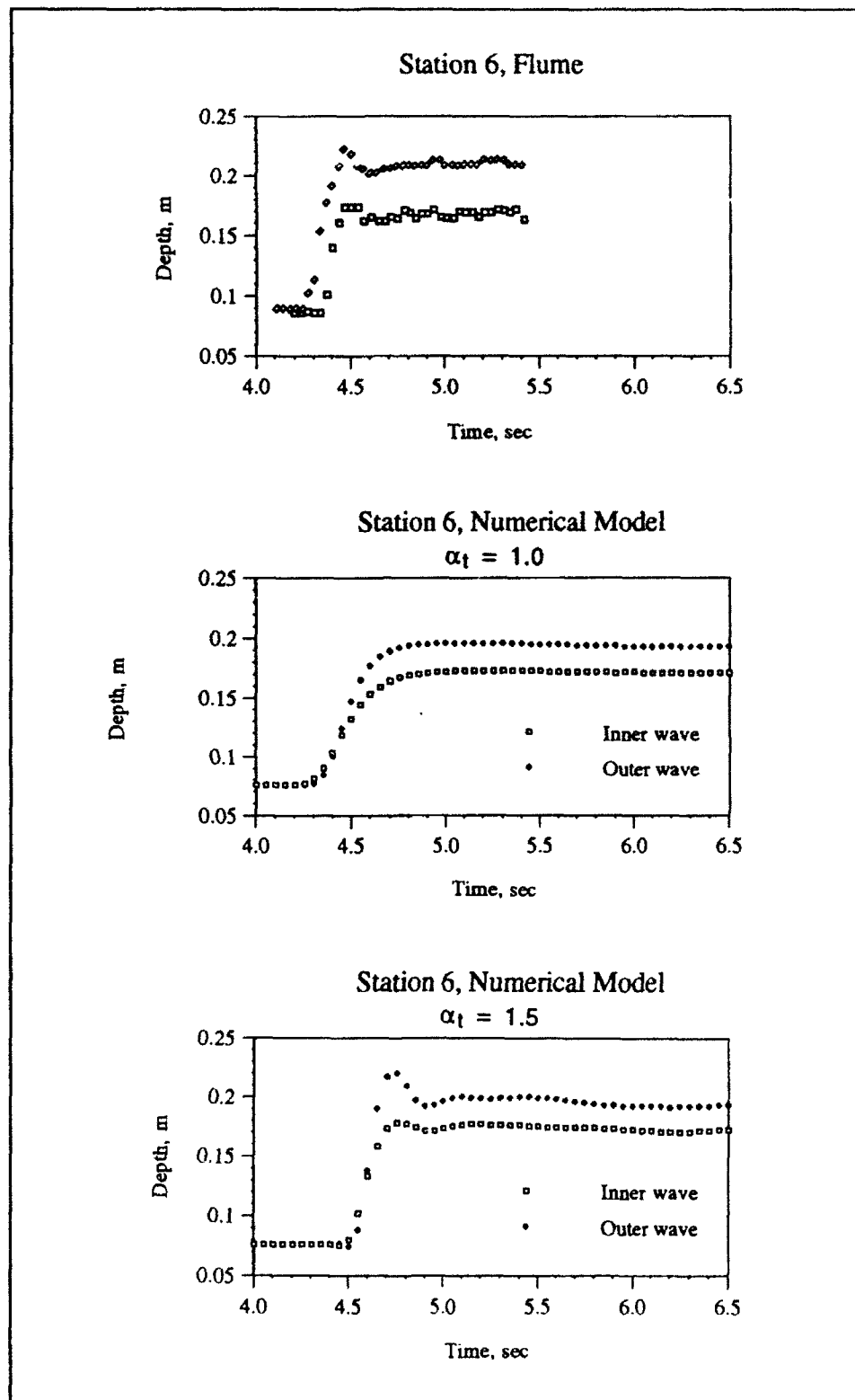


Figure 25. Flume and numerical model depth histories for station 6

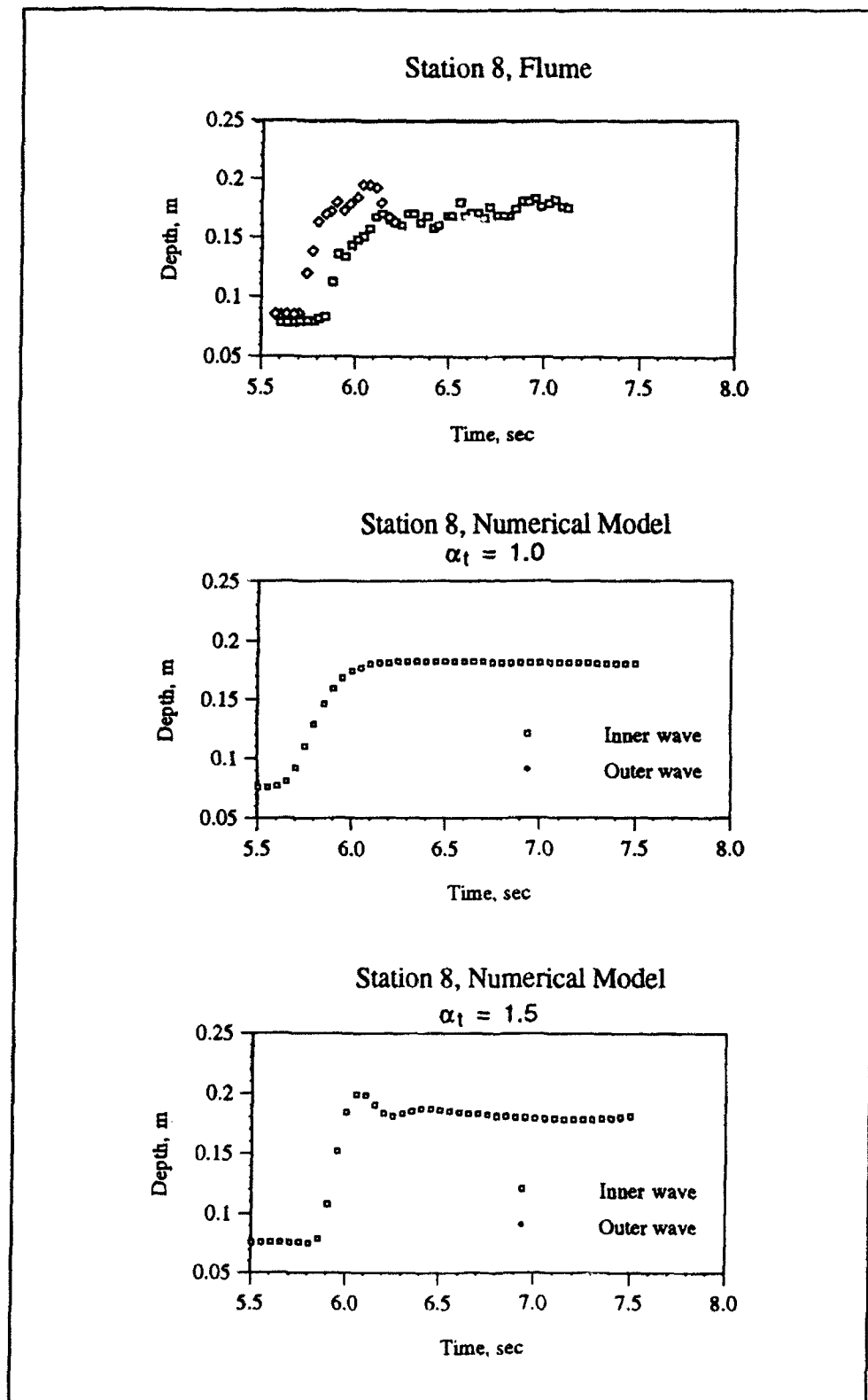


Figure 26. Flume and numerical model depth histories for station 8

With this in mind, stations 4 and 8 match fairly closely between flume and numerical model. Station 4 in the flume would still have a greater difference between outer and inner wave than that predicted by the model. The difference might be a manifestation of a three-dimensional effect that the model cannot mimic. The overall timing and height comparisons are good.

Figure 27 shows the spatial profile of the outer wall water surface elevation of the numerical model versus distance downstream from the dam. These distance measurements are in terms of the center-line distance. The two conditions are for α_t of 1.0 and 1.5, i.e., first- and second-order temporal derivative.

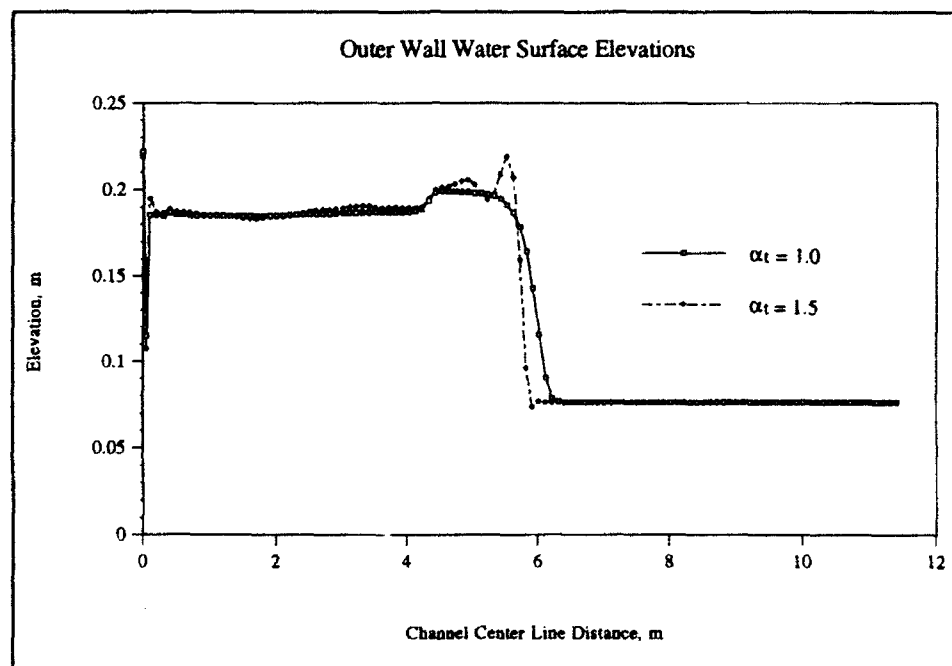


Figure 27. Dam break case water surface elevations, comparison of temporal representation, for time of 3.5 sec

The nodes are delineated by the symbols along the lines. The overshoot of the second-order scheme and the damping of the first-order is obvious. Again, it is probable that the overshoot is a numerical artifact even though this is much like what the flume would show.

Case 3: 2-D Lateral Transition

This is the most geometrically general case that we test. The numerical model is compared to flume results. The flume data was reported in Ippen and Dawson (1951). The tests were conducted for an approach Froude number of 4, upstream depth of 0.1 ft, (0.03048 m) and a total discharge of 1.44 ft³/sec (0.0408 m³/sec). The channel contracts from 2 ft (0.6096 m) to 1 ft

(0.3048 m) wide in a length of 4.78 ft (1.457 m), i.e., an angle of 6 deg on each side.

The model resolution was increased until we were confident that the results no longer changed with greater resolution. The numerical model was set up with 10 evenly spaced elements laterally across the channel and 24 over the length of the transition. The model limits were extended some 40 ft (12.192 m). The total number of nodes was 1661 with 1500 elements. As in the flume test the numerical model was set up to provide a uniform depth of 0.1 ft (0.03048 m) approaching the transition. The bed slope chosen was 0.05664. The other parameters are shown in Table 4.

Table 4 Test Conditions for the Lateral Transition Case	
Condition	Value
α_t	1.0
α, α_s	0.10, 0.50
n	0.0107
v, v_s	0.005, 0.005 ft ² /s (0.0005 m ² /s)
g	32.208 ft/s ² (9.817 m/s ²)
Δt	0.005 sec

Since the model was run to steady-state, α_t of 1.0 is appropriate (time accuracy is irrelevant here).

The results from the numerical model run and the flume results are shown in Figure 28. The oblique shock forms along the sidewalls of the transition and impinges on the point in which the converging channel goes back to parallel walls. This, by the way, is the manner in which one would want to design a lateral transition. The positive wave from the beginning of the converging walls will tend to cancel the negative wave originating at the point where the walls change back to parallel. The heights of the water surface are indicated by the contours in both model and flume. The maximum and minimum heights compare fairly well. The shape is good as well. Generally the wave from the shallow-water equation will be swept downstream less than that from the flume results since the shallow-water equations will transport all wavelengths at the speed of a long wave. Shorter waves will travel more slowly than the shallow-water equations predict. The comparison is good, and the model demonstrates that the shock capturing technique functions well in a general 2-D setting.

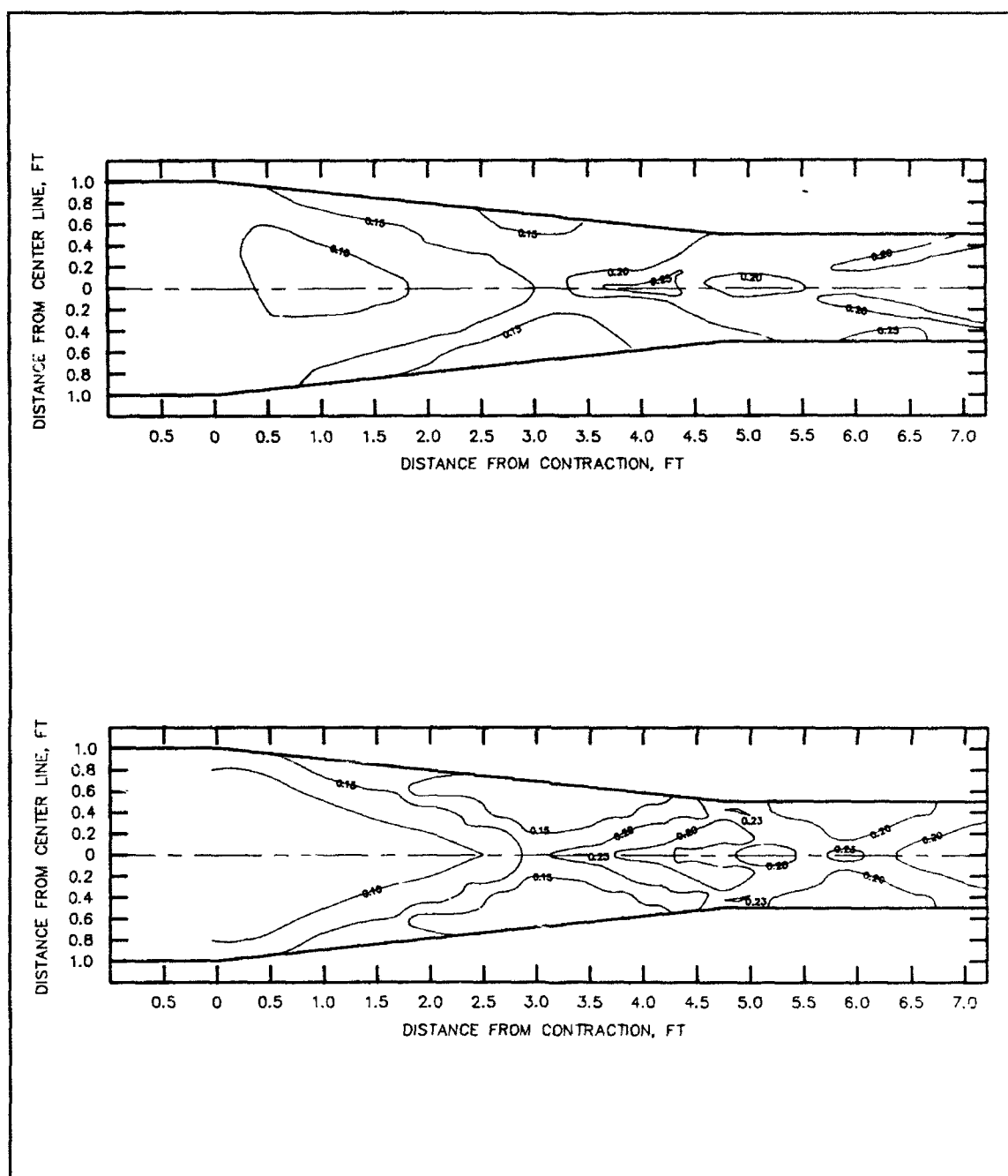


Figure 28. Comparison of flume and numerical model water surface elevations for the supercritical transition case, straight-wall contraction $F = 4.0$. To convert feet to meters, multiply by 0.3048

Discussion

Now let's study the behavior of the 1-D linearized shallow-water equation analytically and numerically. This could lead to a conceptual appreciation of the behavior we have observed in the testing section of the report. We shall follow a Fourier analysis of the wave components; for examples, see Leendertse (1967) or Froehlich (1985). First let's consider the nondimensionalized shallow-water equations

$$\frac{\partial Q_*}{\partial t_*} + \begin{bmatrix} 0 & 1 \\ 1-F_o^2 & 2F_o \end{bmatrix} \frac{\partial Q_*}{\partial x_*} = 0 \quad (54)$$

where, the subscript * indicates nondimensional quantities and o as a subscript indicates a constant, and

$$F_o = |U_o/C_w|$$

$$C_w = (gh_o)^{(1/2)}$$

$$Q_* = \begin{bmatrix} h/h_o \\ P/(C_w h_o) \end{bmatrix}$$

These equations can be diagonalized by defining a new variable

$$T = P_o^{-1} Q_* \quad (55)$$

such that $P_o^{-1} A_o P_o = \Lambda_o$

where

$$A_o = \begin{bmatrix} 0 & 1 \\ 1-F_o^2 & 2F_o \end{bmatrix}$$

$$\Lambda_o = \begin{bmatrix} F_o+1 & 0 \\ 0 & F_o-1 \end{bmatrix} = \begin{bmatrix} \lambda_1 & 0 \\ 0 & \lambda_2 \end{bmatrix}$$

$$P_o = \begin{bmatrix} \lambda_2 & -1 \\ \lambda_1 & -1 \end{bmatrix} ; \quad P_o^{-1} = \frac{1}{2} \begin{bmatrix} -1 & 1 \\ -\lambda_1 & \lambda_2 \end{bmatrix}$$

Λ_o is the diagonal matrix of eigenvalues and P_o and P_o^{-1} are composed of the eigenvectors (and are arbitrary). With the substitution of Equation 55 into 54 and multiplication by P_o^{-1} we retrieve the diagonalized shallow-water equations in terms of the Riemann Invariants

$$\frac{\partial T}{\partial t_*} + \Lambda_o \frac{\partial T}{\partial x_*} = 0 \quad (56)$$

Now if we consider solutions in terms of

$$T(x,t) = \hat{T} e^{\gamma t} e^{iKx} \quad (57)$$

where \hat{T} is a constant and K is the wave number, we arrive at the solution

$$T(x,t) = \hat{T} e^{i(Kx - \omega t)} \quad (58)$$

where

$$\begin{aligned} \omega &= K\lambda, \text{ the wave frequency} \\ \gamma &= -i\omega \end{aligned}$$

With this solution we shall now compare the behavior of the model to that of the analytic solution.

The test function for Equation 54 in HIVEL2D would be

$$\psi_i I = \phi_i I + \alpha \Delta x P_o^{-1} |\Lambda_o| \Lambda_o^{-1} P_o \frac{\partial \phi_i}{\partial x} \quad (59)$$

Now, since T is a linear combination of the variables h_* and P_* we can convert this to the diagonal system as well, so that the equivalent test function is

$$\psi_i I = \phi_i I + \alpha \Delta x |\Lambda_o| \Lambda_o^{-1} \frac{\partial \phi_i}{\partial x} \quad (60)$$

Applying this test function to the discretized differential equation and substituting

$$T(x) = \sum_j \phi_j(x) T_j$$

and

$$T_j^n = \hat{T} e^{-in\Delta t\omega} e^{ij\Delta xK}$$

where the superscript n indicates the time-step and the subscript j is the spatial node location.

We now present the results of this analysis for $\alpha = 1/2$ and for the temporal derivative parameter α_t of 1.0 and 1.5. We shall compare the relative amplitude and relative speed for a single time-step. The parameter for relative speed is given by

$$\text{relative speed} = \frac{\tan^{-1} \frac{\operatorname{Im} \left(e^{-i \frac{2\pi}{N}} \right)}{\operatorname{Re} \left(e^{-i \frac{2\pi}{N}} \right)}}{\frac{2\pi}{N} C} \quad (61)$$

where

N = elements per wavelength

$$C = \text{Courant number} = \frac{\lambda \Delta t_*}{\Delta x_*}$$

λ = wave speed, either λ_1 or λ_2

For $\alpha_t = 1$, which is first-order backward difference in time, the relative amplitude is shown in Figure 29 and the relative wave speed is shown in Figure 30. This is plotted versus the number of elements per wavelength N and the Courant number C . Also remember that these comparisons apply for either characteristic (λ_1 or λ_2), even for subcritical conditions in which λ_2 is negative. In these figures the Courant number varies from 0.5 to 2.0 and the elements per wavelength from 2 to 10.

The amplitude portrait shows substantial damping for larger C and for the shorter wavelengths (or alternatively the poorer resolution). The large damping at a wavelength of $2\Delta x$ is important, as this is the mechanism that provides the energy dissipation to capture shocks. Now consider the phase portrait, or in this case the relative speed portrait. Over the conditions shown, the numerical speed is less than the analytic speed throughout. For larger C the relative speed is somewhat lower (worse). For $N = 2$ the speed is 0, so that undamped oscillation could remain at steady state.

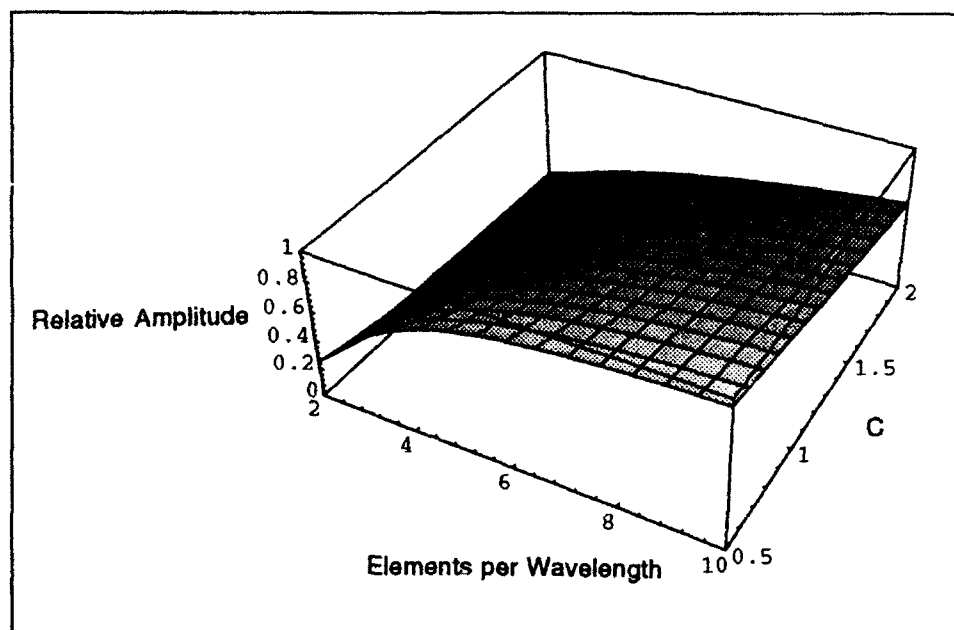


Figure 29. Relative amplitude versus C and resolution for $\alpha_f = 1.0$ and $\alpha = 0.5$

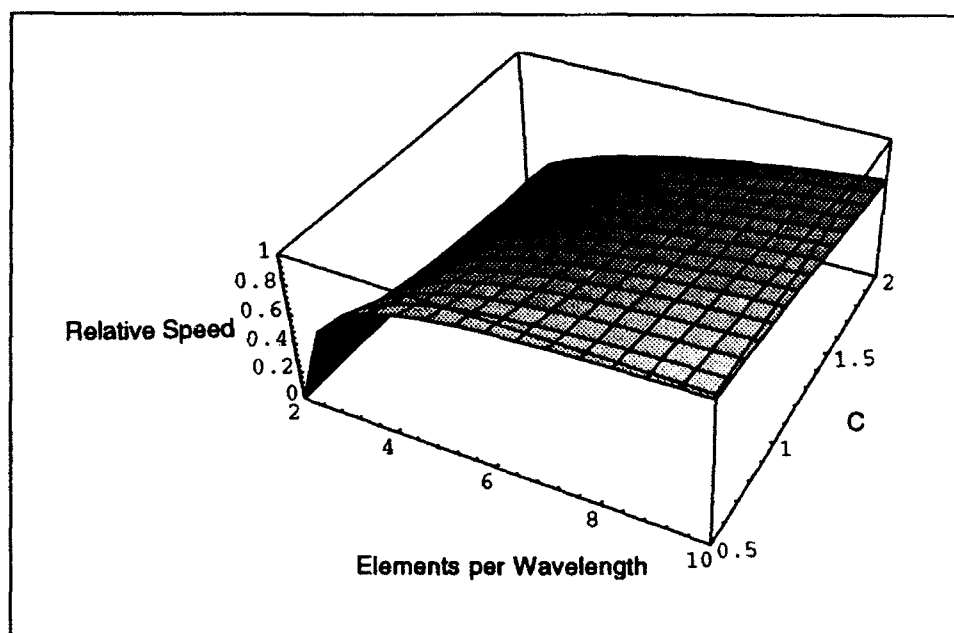


Figure 30. Relative speed versus C and resolution for $\alpha_f = 1.0$ and $\alpha = 0.5$

In comparison to the results we have shown in Figures 6-11 for Case 1, analytic shock case, we must remember that C_s is the Courant number based on shock speed, whereas C is based on the perturbation wave speed. If we consider a wave moving upstream just behind the shock, since short wavelengths move too slowly, the disturbance of the shock produces waves of these length which fall behind the shock rather than remaining within. As the time-step is reduced (C_s gets smaller) the relative speed is better for the moderate wavelengths and so the shock front becomes sharper.

At a point near the shock front we note that generally we get a sharp front with no undershoot until we reach the smallest time-step. Again if we are within the shock at a depth where there is an upstream propagating wave (subcritical), is there a Courant number C that has a relative speed greater than analytic. This would be the only way in which an undershoot could appear. Figure 31 extends the relative wave speed portrait below $C = 0.5$. From this figure it is apparent for small values of C that the numerical wave speed is greater than analytic so that it is possible to develop an undershoot in front of the jump.

For $\alpha_t = 1.5$ we have a second-order temporal derivative which has relative amplitude and relative speed portraits shown in Figures 32 and 33, respectively. The degree of damping is much less than for the first-order case. The relative speed is better but not so dramatic as the improvement in amplitude. An interesting point is that the relative speed for $N = 2$ is nonzero for lower C values. This implies that a spurious mode should not reside in the grid at steady state. In Figure 34, we show the relative speed portrait extended below C values of 0.5. As with $\alpha_t = 1$, for very low C the numerical relative speed is greater than the analytic. Therefore, we would expect to have an undershoot for small time-steps. It should become more pronounced and longer as the time-step is reduced further. Since we generally have a relative speed lower than analytic, we expect an overshoot behind the jump which becomes longer as the time-step is increased. Referring to Figures 14-19 of case 1, this is precisely what we note. Also, for smaller time-steps there is some undershoot as well. These same features are notable in the second test case, the dam break test case.

For the sake of completeness the relative amplitude and speed portraits are included for $\alpha = 0$ and 0.25 at α_t of 1.0 and 1.5 in Figures 35-42. The condition $\alpha = 0$ is, in fact, the Galerkin case since the Petrov-Galerkin contribution is included through α . The Galerkin approach is shown to contain a steady-state spurious mode due to the speed of zero for $N = 2$. Furthermore, this mode is undamped. The case of $\alpha = 0.25$ shows that the relative speed portraits change very little from $\alpha = 0.5$ but the amplitude damping is improved.

The obvious conclusions that can be drawn from this discussion is that for an unsteady run either use $\alpha_t = 1.5$ or take smaller time-steps with $\alpha_t = 1.0$. An improvement in spatial resolution dramatically improves the solution.

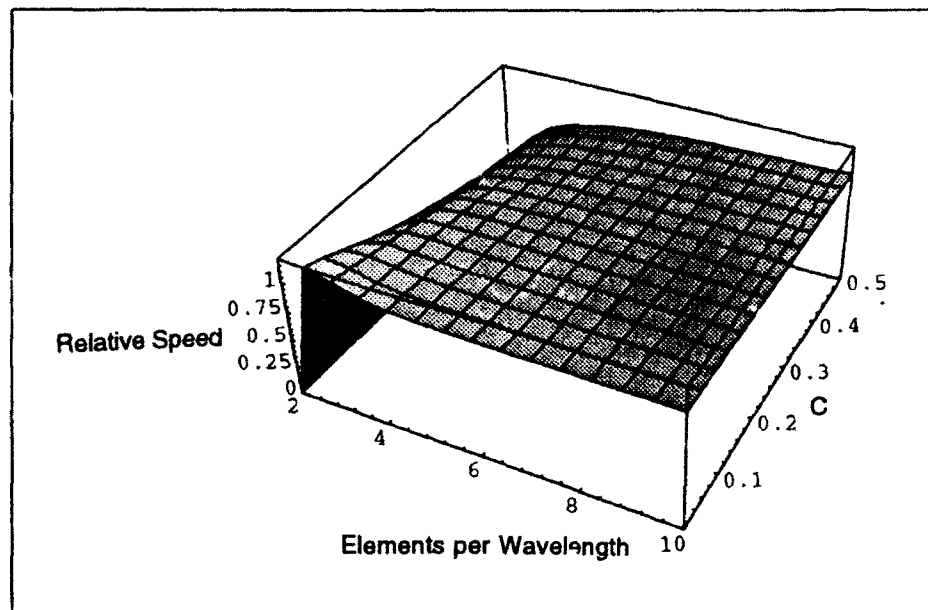


Figure 31. Relative speed versus C and resolution for $\alpha_f = 1.0$ and $\alpha = 0.5$, for small values of C

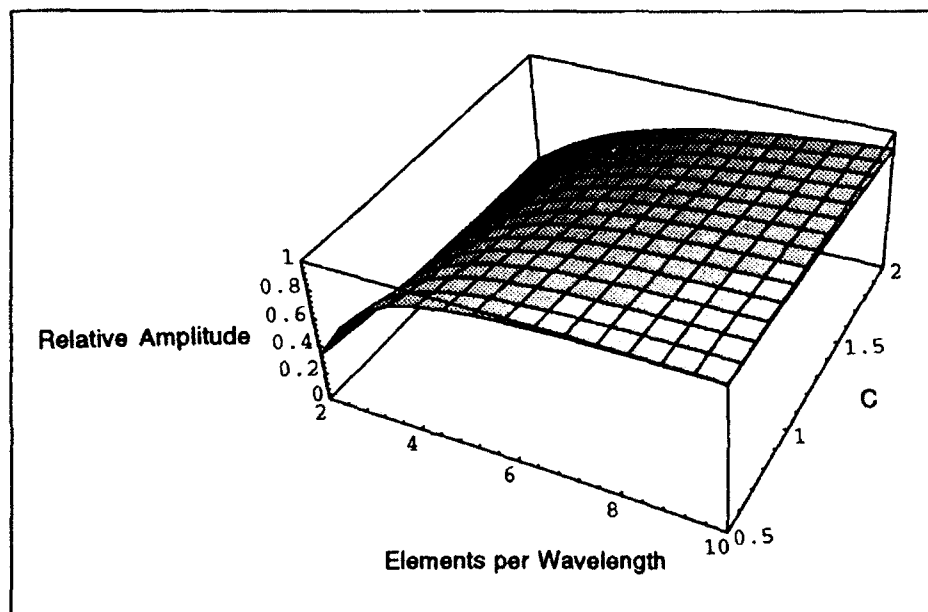


Figure 32. Relative amplitude versus C and resolution for $\alpha_f = 1.5$ and $\alpha = 0.5$

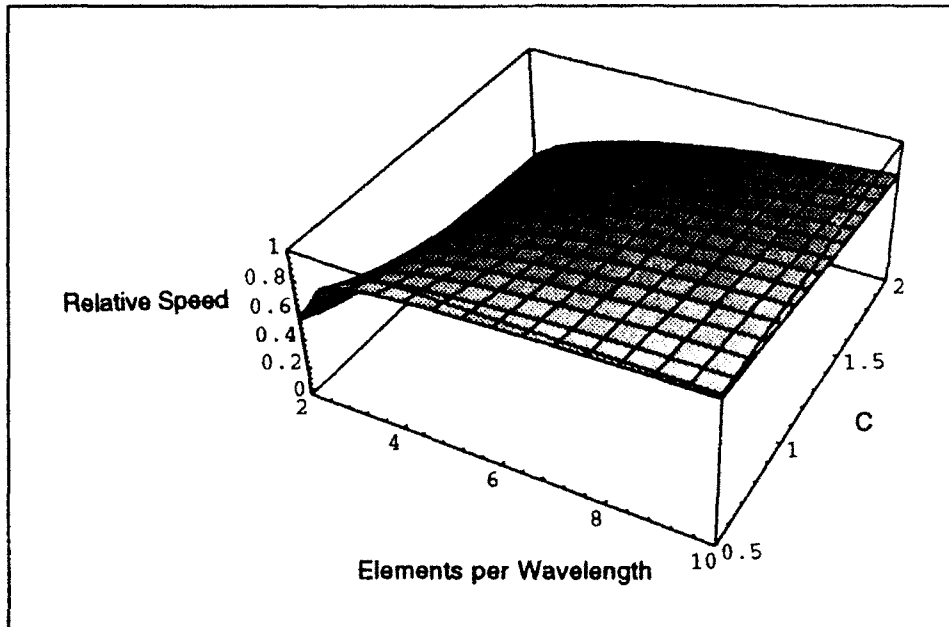


Figure 33. Relative speed versus C and resolution for $\alpha_t = 1.5$ and $\alpha = 0.5$

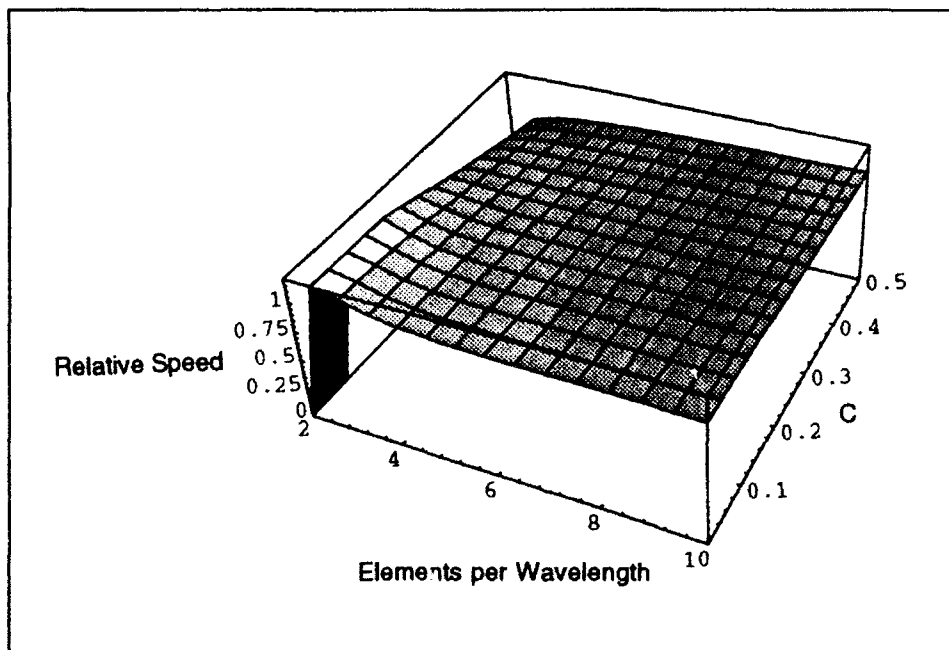


Figure 34. Relative speed versus C and resolution for $\alpha_t = 1.5$ and $\alpha = 0.5$, for small values of C

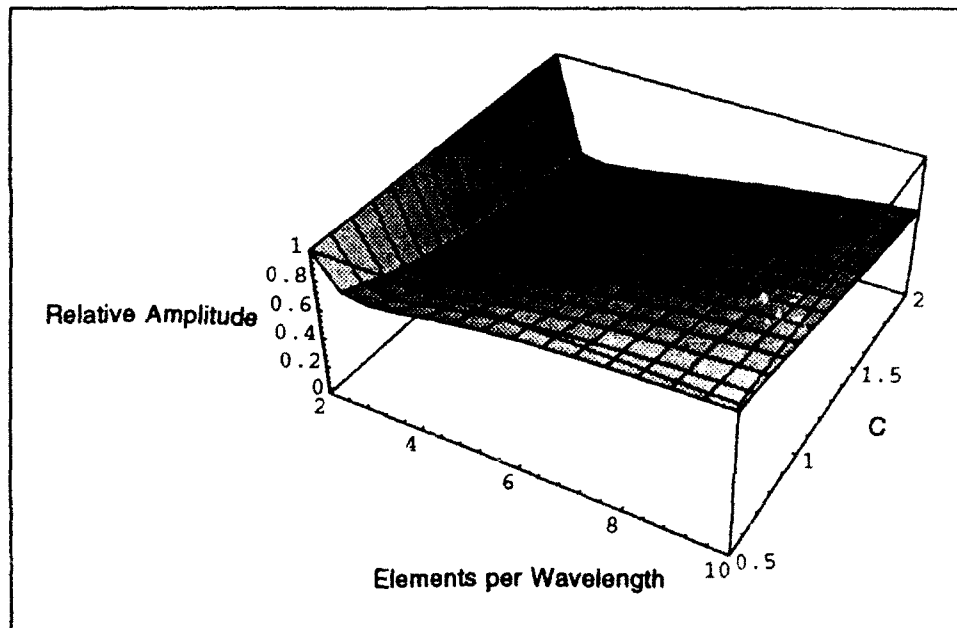


Figure 35. Relative amplitude versus C and resolution for $\alpha_t = 1.0$ and $\alpha = 0$

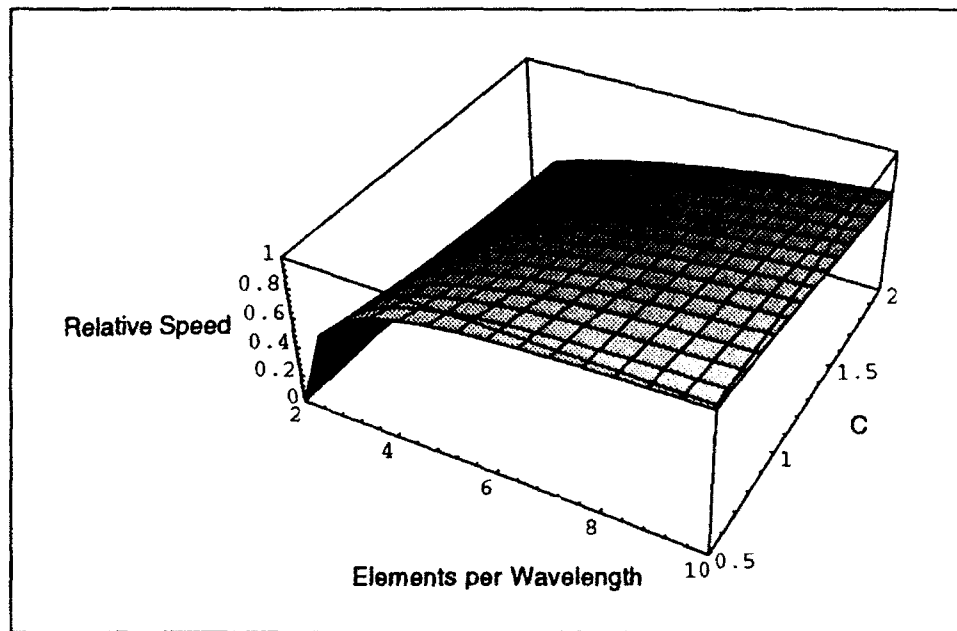


Figure 36. Relative speed versus C and resolution for $\alpha_t = 1.0$ and $\alpha = 0$

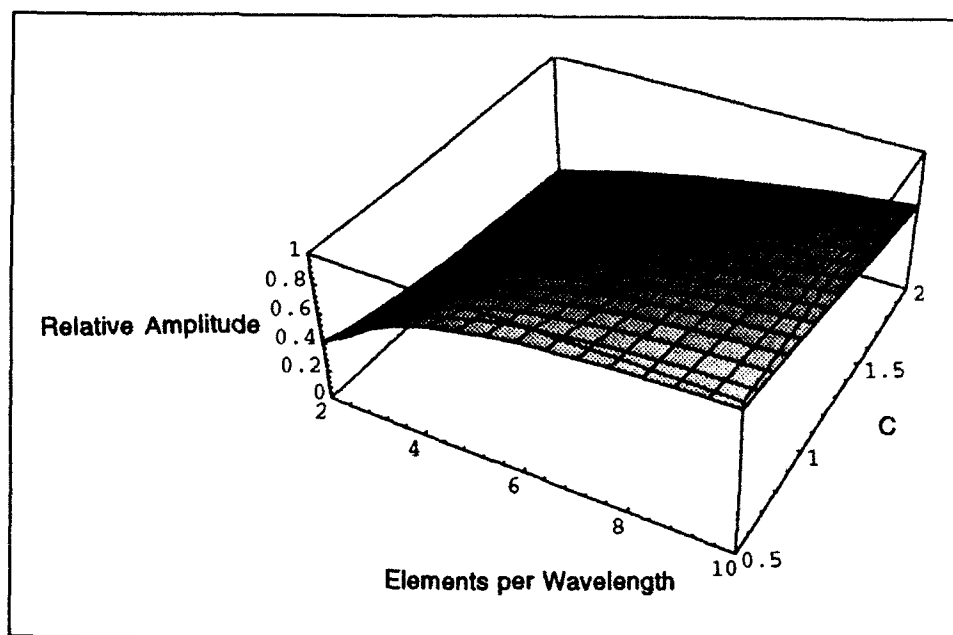


Figure 37. Relative amplitude versus C and resolution for $\alpha_t = 1.0$ and $\alpha = 0.25$

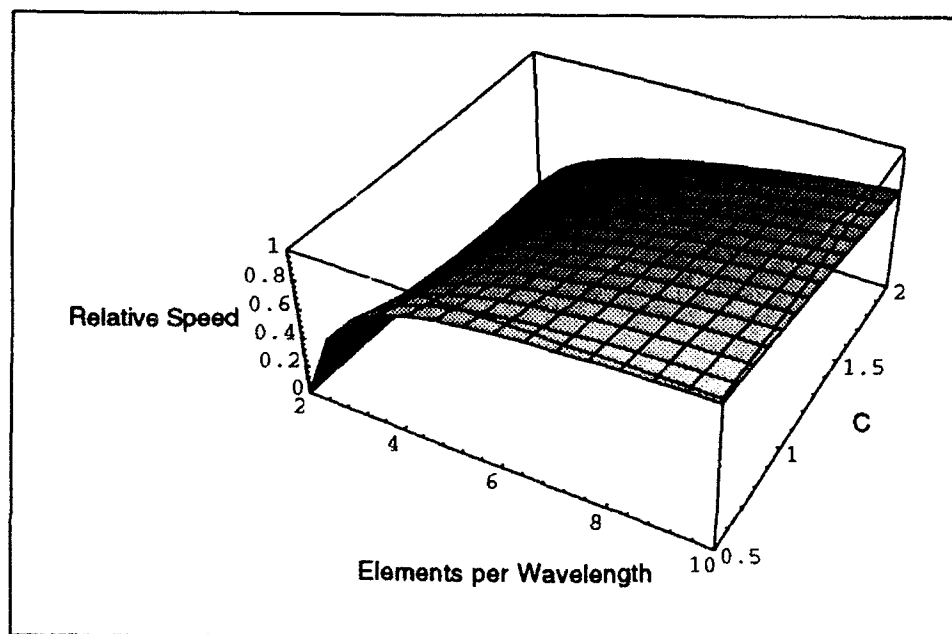


Figure 38. Relative speed versus C and resolution for $\alpha_t = 1.0$ and $\alpha = 0.25$

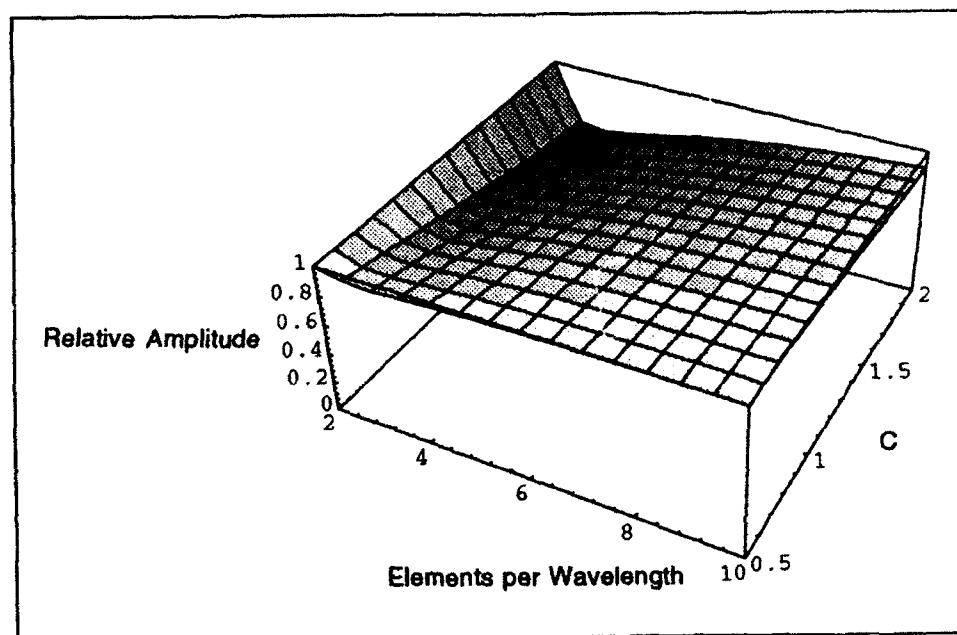


Figure 39. Relative amplitude versus C and resolution for $\alpha_f = 1.5$ and $\alpha = 0$

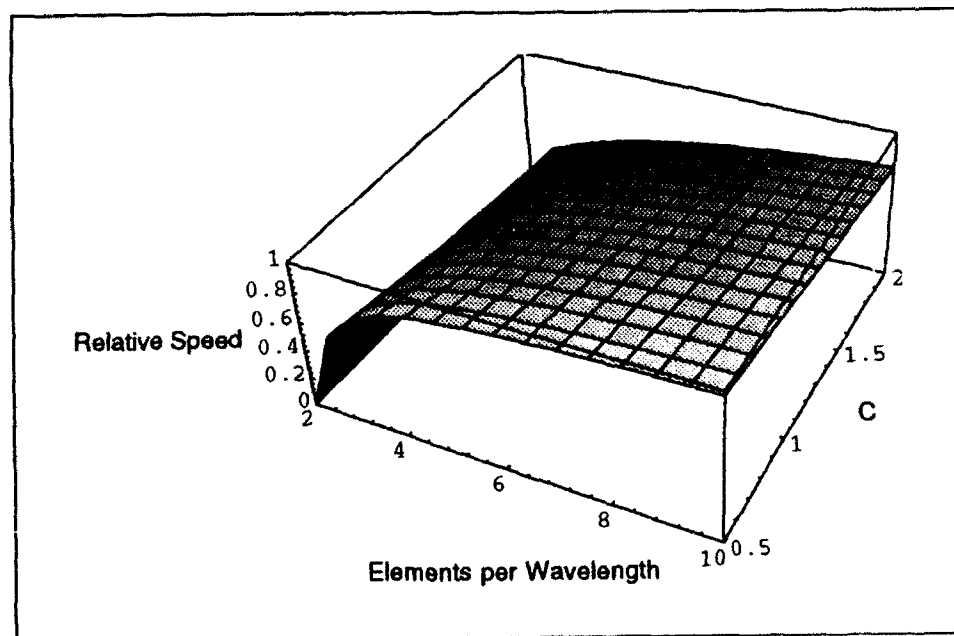


Figure 40. Relative speed versus C and resolution for $\alpha_f = 1.5$ and $\alpha = 0$

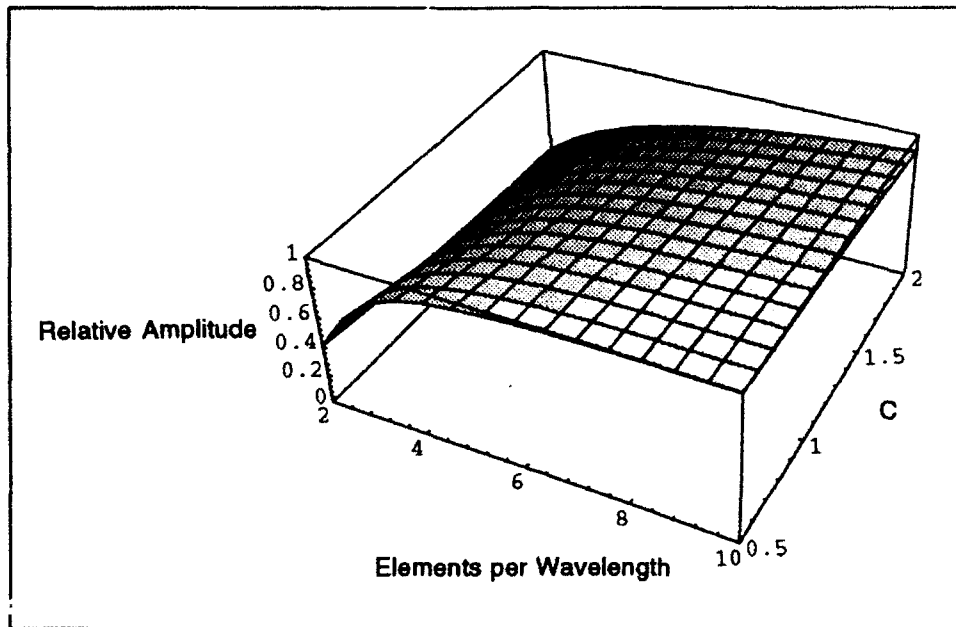


Figure 41. Relative amplitude versus C and resolution for $\alpha_t = 1.5$ and $\alpha = 0.25$

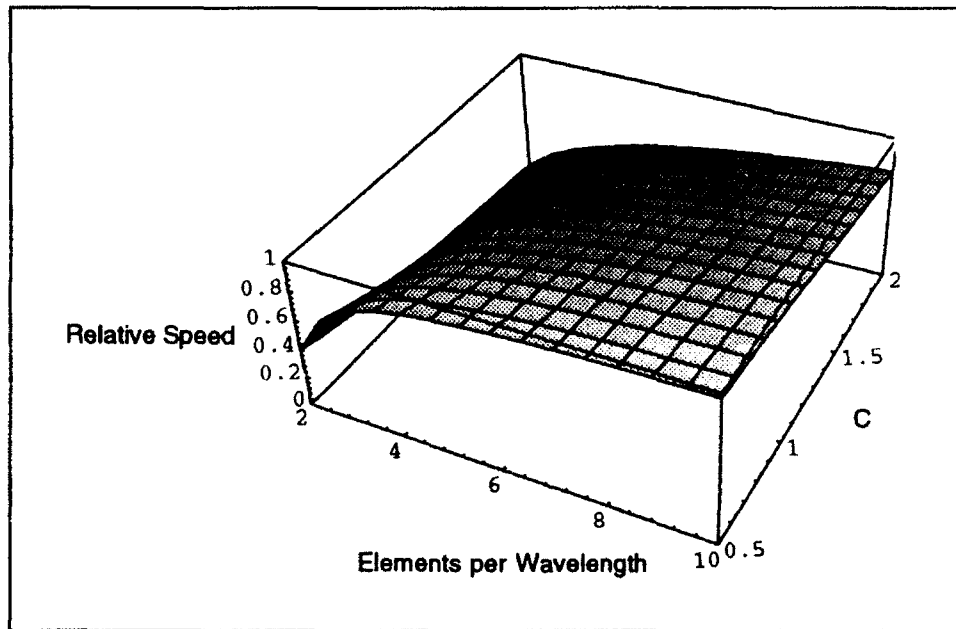


Figure 42. Relative speed versus C and resolution for $\alpha_t = 1.5$ and $\alpha = 0.25$

4 Conclusions

In this report an algorithm is developed to address the numerical difficulties in modeling surges and jumps in a computational hydraulics model. The model itself is a finite element computer code representing the 2-D shallow water equations.

The technique developed to address the case of advection-dominated flow is a dissipative technique that serves well for the capturing of shocks. The dissipative mechanism is large for short wavelengths, thus enforcing energy loss through the hydraulic jump, unlike a nondissipative technique used on C^0 representation of depth, which will implicitly enforce energy conservation, dictated by the shallow-water equations, through a $2\Delta x$ oscillation.

The test cases demonstrate that the resulting model converges to the correct heights and shock speeds with increasing resolution. Furthermore, general 2-D cases of lateral transition in supercritical flow showed the model to compare quite well in reproducing the oblique shock pattern.

The trigger mechanism, based upon energy variation, appears to detect the jump quite well. The Petrov-Galerkin technique shown is an intuitive method relying upon characteristic speeds and directions and produces a 2-D model which is adequate to address hydraulic problems involving jumps and oblique shocks.

The resulting improved numerical model will have application in supercritical as well as subcritical channels, and transitions between regimes. The model can determine the water surface heights along channels and around bridges, confluences, and bends for a variety of numerically challenging events such as hydraulic jumps, hydropower surges, and dam breaks. Furthermore, the basic concepts developed are applicable to models of aerodynamic flow fields, providing enhanced stability in calculation of shocks on engine or helicopter rotors, for example, as well as on high-speed aircraft.

References

- Anderson, D. A., Tannehill, J. C., and Pletcher, R. H. (1984). *Computational fluid mechanics and heat transfer*. Hemisphere Publishing, Washington, DC.
- Bell, S. W., Elliot, R. C., and Chaudhry, M. H. (1992). "Experimental results of two-dimensional dam-break flows," *Journal of Hydraulic Research* 30(2), 225-252.
- Berger, R. C. (1992). "Free-surface flow over curved surfaces," Ph.D. diss., University of Texas at Austin.
- Berger, R. C., and Winant, E. H. (1991). "One dimensional finite element model for spillway flow." *Hydraulic Engineering*, Proceedings, 1991 National Conference, ASCE, Nashville, Tennessee, July 29-August 2, 1991. Richard M. Shane, ed., New York, 388-393.
- Courant, R., and Friedrichs, K. O. (1948). *Supersonic flow and shock waves*, Interscience Publishers, New York, 121-126.
- Courant, R., Isaacson, E., and Rees, M. (1952). "On the solution of nonlinear hyperbolic differential equations," *Communication on Pure and Applied Mathematics* 5, 243-255.
- Dendy, J. E. (1974). "Two methods of Galerkin-type achieving optimum L^2 rates of convergence for first-order hyperbolics," *SIAM Journal of Numerical Analysis* 11, 637-653.
- Froehlich, D. C. (1985). Discussion of "A dissipative Galerkin scheme for open-channel flow," by N. D. Katopodes, *Journal of Hydraulic Engineering*, ASCE, 111(4), 1200-1204.
- Gabutti, B. (1983). "On two upwind finite different schemes for hyperbolic equations in non-conservative form," *Computers and Fluids* 11(3), 207-230.
- Hicks, F. E., and Steffler, P. M. (1992). "Characteristic dissipative Galerkin scheme for open-channel flow," *Journal of Hydraulic Engineering*, ASCE, 118(2), 337-352.

- Hughes, T. J. R., and Brooks, A. N. (1982). "A theoretical framework for Petrov-Galerkin methods with discontinuous weighting functions: Applications to the streamline-upwind procedures." *Finite Elements in Fluids*, R. H. Gallagher, et al., ed., J. Wiley and Sons, London, 4, 47-65.
- Ippen, A. T., and Dawson, J. H. (1951). "Design of channel contractions," *High-velocity flow in open channels: A symposium*. Transactions ASCE, 116, 326-346.
- Katopodes, N. D. (1986). "Explicit computation of discontinuous channel flow," *Journal of Hydraulic Engineering*, ASCE, 112(6), 456-475.
- Keulegan, G. H. (1950). "Wave motion." *Engineering Hydraulics*, Proceedings, Fourth Hydraulics Conference, Iowa Institute of Hydraulic Research, June 12-15, 1949. Hunter Rouse, ed., John Wiley and Sons, New York, 748-754.
- Leendertse, J. J. (1967). "Aspects of a computational model for long-period water-wave propagation," Memorandum RM 5294-PR, Rand Corporation, Santa Monica, CA.
- Moretti, G. (1979). "The λ -scheme," *Computers in Fluids* 7(3), 191-205.
- Platzman, G. W. (1978). "Normal modes of the world ocean; Part 1, Design of a finite element barotropic model," *Journal of Physical Oceanography* 8, 323-343.
- Steger, J. L., and Warming, R. F. (1981). "Flux vector splitting of the inviscid gas dynamics equations with applications to finite difference methods," *Journal of Computational Physics* 40, 263-293.
- Stoker, J. J. (1957). *Water waves: The mathematical theory with applications*. Interscience Publishers, New York, 314-326.
- Von Neumann, J., and Richtmyer, R. D. (1950). "A method for the numerical calculation of hydrodynamic shocks," *Journal of Applied Physics* 21, 232-237.
- Walters, R. A., and Carey, G. F. (1983). "Analysis of spurious oscillation modes for the shallow water and Navier-Stokes equations," *Journal of Computers and Fluids*, 11(1), 51-68.

REPORT DOCUMENTATION PAGE			Form Approved OMB No. 0704-0188	
Public reporting burden for this collection of information is estimated to average 1 hour per response, including the time for reviewing instructions, searching existing data sources, gathering and maintaining the data needed, and completing and reviewing the collection of information. Send comments regarding this burden estimate or any other aspect of this collection of information, including suggestions for reducing this burden, to Washington Headquarters Services, Directorate for Information Operations and Reports, 1215 Jefferson Davis Highway, Suite 1204, Arlington, VA 22202-4302, and to the Office of Management and Budget, Paperwork Reduction Project (0704-0188), Washington, DC 20503.				
1. AGENCY USE ONLY (Leave blank)		2. REPORT DATE August 1993		3. REPORT TYPE AND DATES COVERED Final report
4. TITLE AND SUBTITLE A Finite Element Scheme for Shock Capturing			5. FUNDING NUMBERS	
6. AUTHOR(S) R. C. Berger				
7. PERFORMING ORGANIZATION NAME(S) AND ADDRESS(ES) U.S. Army Engineer Waterways Experiment Station Hydraulics Laboratory 3909 Halls Ferry Road, Vicksburg, MS 39180-6199			8. PERFORMING ORGANIZATION REPORT NUMBER Technical Report HL-93-12	
9. SPONSORING / MONITORING AGENCY NAME(S) AND ADDRESS(ES) Assistant Secretary of the Army (R&D) Washington, DC 20315			10. SPONSORING / MONITORING AGENCY REPORT NUMBER	
11. SUPPLEMENTARY NOTES Available from National Technical Information Service, 5285 Port Royal Road, Springfield, VA 22161.				
12a. DISTRIBUTION / AVAILABILITY STATEMENT Approved for public release; distribution is unlimited.			12b. DISTRIBUTION CODE	
13. ABSTRACT (Maximum 200 words) The representation of hydraulic jumps or shocks in compressible fluids is a difficult task for numerical models. These models require more smoothness than the analytic solution contains. For this reason these models are plagued with oscillations. The most widespread method is to smear the solution in the vicinity of the shock, giving up $O(1)$ errors, but restricting the error to the neighborhood of the jump or shock. This technique is called shock-capturing. In this report a method to capture hydraulic jumps formed by the shallow-water equations in a finite element model is demonstrated. The model itself is two-dimensional. The method it relies upon is a Petrov-Galerkin approach in which the degree of upstream bias in the test function is based upon the characteristics of the convection matrix. Furthermore, in order to restrict the shock capturing to the vicinity of the jump, a method of jump detection is implemented which depends on the variation of mechanical energy within an element. The veracity of the model is tested by comparison of the predicted jump speed and magnitude with analytic and flume results. A comparison is also made to a flume case of steady-state supercritical lateral transition.				
14. SUBJECT TERMS Characteristics Petrov-Galerkin supercritical finite element shallow-water equations two-dimensional hydraulic jump shock capturing			15. NUMBER OF PAGES 61	
			16. PRICE CODE	
17. SECURITY CLASSIFICATION OF REPORT UNCLASSIFIED	18. SECURITY CLASSIFICATION OF THIS PAGE UNCLASSIFIED	19. SECURITY CLASSIFICATION OF ABSTRACT	20. LIMITATION OF ABSTRACT	